Materials Today Communications

Molecular Dynamics Simulations of Nanoparticle Sintering in Additive Nanomanufacturing: The Role of Particle Size, Misorientation Angle, Material Type, and Temperature --Manuscript Draft--

Manuscript Number:	MTCOMM-D-24-03239		
Article Type:	Full Length Article		
Section/Category:	Nanomaterials		
Keywords:	Additive nanomanufacturing; Additive manufacturing; Sintering; Nanoparticles; Molecular dynamics		
Corresponding Author:	Shuai Shao Auburn University Auburn, AL UNITED STATES		
First Author:	Dourna Jamshideasli		
Order of Authors:	Dourna Jamshideasli		
	Masoud Mahjouri-Samani		
	Nima Shamsaei		
	Shuai Shao		
Abstract:	Additive nanomanufacturing, where nanoparticles (NPs) are generated via laser material ablation and sintered via laser, permits the fabrication of novel electronic devices with adequate flexibility, such as tunable material composition, adjustable sintered state, and a wide selection of substrates—including biodegradable ones—to name a few. The laser energy input often needs to be carefully balanced between achieving adequate sintering and avoiding substrate damage. The sintered state of NPs, a key influencing factor of the resistivity of electronic circuits, depends not only on temperature (the result of laser energy input), but also on NPs size, size ratio, and crystallographic misorientation. While the minuteness of NPs and the transient nature of their sintering (typically within a nanosecond) make direct experimental evaluation of such parameters challenging, the length and time scales are uniquely suitable for molecular dynamic (MD) studies. This study utilizes MD to investigate the sintering characteristics of silver and copper NP doublets at different temperatures and examines the effects of NP size, size ratios, misorientation angle (including both tilt and twist), and material type. A mathematical framework to describe the characteristic sintering time, i.e., time needed for a NP doublet to achieve a given normalized neck size, was proposed based on MD results.		
Suggested Reviewers:	Mina Yoon Oak Ridge National Laboratory myoon@ornl.gov		
	Jesse M Sestito Valparaiso University jesse.sestito@valpo.edu		
	Fadi Abdeljawad Lehigh University fadi@lehigh.edu		
	Tequila AL Harris Georgia Institute of Technology tequila.harris@me.gatech.edu		
Opposed Reviewers:			

(Title page)

Molecular Dynamics Simulations of Nanoparticle Sintering in Additive Nanomanufacturing: The Role of Particle Size, Misorientation Angle, Material Type, and Temperature

Dourna Jamshideasli^{1,2}, Masoud Mahjouri-Samani^{1,3}, Nima Shamsaei^{1,2}, Shuai Shao^{1,2*}

¹ National Center for Additive Manufacturing Excellence (NCAME), Auburn University, Auburn, AL 36849, USA

² Department of Mechanical Engineering, Auburn University, Auburn, AL 36849, USA

³ Department of Electrical and Computer Engineering, Auburn University, Auburn, AL 36849, USA

*Corresponding author: sshao@auburn.edu

Phone: (334) 844-4820

Submitting to:

Materials Today Communications

February 2024

Highlights

- Sintering of silver and copper monometallic nanoparticles (NPs) are simulated by MD
- Role of particle size, misorientation, and temperature in NP sintering are examined
- Evolution of interparticle neck size is analyzed to examine sintering effectiveness
- Both tilt and twist grain boundaries are found to expedite sintering
- Higher temperature, smaller and uneven NPs are all beneficial for effective sintering

Abstract

Additive nanomanufacturing, where nanoparticles (NPs) are generated via laser material ablation and sintered via laser, permits the fabrication of novel electronic devices with adequate flexibility, such as tunable material composition, adjustable sintered state, and a wide selection of substrates—including biodegradable ones—to name a few. The laser energy input often needs to be carefully balanced between achieving adequate sintering and avoiding substrate damage. The sintered state of NPs, a key influencing factor of the resistivity of electronic circuits, depends not only on temperature (the result of laser energy input), but also on NPs size, size ratio, and crystallographic misorientation. While the minuteness of NPs and the transient nature of their sintering (typically within a nanosecond) make direct experimental evaluation of such parameters challenging, the length and time scales are uniquely suitable for molecular dynamic (MD) studies. This study utilizes MD to investigate the sintering characteristics of silver and copper NP doublets at different temperatures and examines the effects of NP size, size ratios, misorientation angle (including both tilt and twist), and material type. A mathematical framework to describe the characteristic sintering time, i.e., time needed for a NP doublet to achieve a given normalized neck size, was proposed based on MD results.

Keywords:

Additive nanomanufacturing; Additive manufacturing; Sintering; Nanoparticles; Molecular dynamics

Abbreviations and nomenclature

ANM	Additive nanomanufacturing
NPs	Nanoparticles
MD	Molecular dynamics
FCC	Face-centered cubic
НСР	Hexagonal closed packed
EAM	Embedded atom method
VMD	Visual molecular dynamics
LAMMPS	Large-scale atomic/molecular massively parallel simulator
OVITO	Open visualization tool
GB	Grain boundary
L_0	Initial center-to-center distance
L	Center-to-center distance
T	Absolute temperature
T_m	Bulk melting temperature
D	Diameter of the (larger) NP
d	Diameter of the smaller NP
D_{eq}	Equivalent diameter
k	Boltzmann constant
$\frac{J_0}{J}$	Pre-exponential factor
J	Rate of diffusion
S	Neck size
t	Time
t_{ch}	Characteristic time
$\frac{t_{ch}}{E_a}$	Activation energy
ρ	Radius of the neck surface
Ψ	Dihedral angle

1. Introduction

Recent research [1–5] has led to the development of biodegradable flexible electronic devices such as "papertronics". These devices are based on paper substrates that are degradable and water-soluble, making them more sustainable and eco-friendly. Production, deposition, and sintering of nanoparticles (NPs) are critical steps in dry printing electronic devices on these temperature-sensitive and water-soluble substrates. On-demand generation of NPs has been recently achieved by pulsed laser ablation of solid targets under argon background pressure [2], leading to laser-based single step additive nanomanufacturing (ANM). Laser sintering of these NPs [6], has been shown to join them together, forming desired patterns and structures on substrates. While supplying sufficient laser energy is required to minimize the electrical resistivity of the printed lines, it is traded off with the risk of substrate damage [7], making fine-tuning the laser parameters a challenging task. Indeed, since the sintering dynamics for NPs are still not well-understood, such tuning presently proceeds in a trial-and-error manner.

Sintering of micro particles is central to several key industrial sectors, such as ceramics and powder metallurgy, and has spurred significant research interest. As a result, several key factors governing sintering rates have been identified, including temperature, material type, particle size, size ratio, and misorientation. As a solid-state process, particle sintering primarily relies on the diffusional transport of mass from the particle interior/surface to the inter-particle neck via various paths, including lattice, surface, and grain boundaries (GBs), etc. Accordingly, these factors govern sintering by influencing diffusion. For instance, a higher temperature facilitates more effective sintering since temperature positively affects diffusion rates. At room temperature, the sintering of micro particles may not occur at all [8]. Sintering is generally easier for materials with lower cohesive energies, such as noble metals [9], since these materials tend to have lower

activation energies for diffusion. In addition, the sintering paths within smaller particles are shorter. Therefore, the sintering of smaller particles generally tends to be more effective and can occur at a lower temperature than larger ones [9]. When the particles being sintered have very different sizes (e.g., beyond 50% difference in diameters), sintering is typically more effective than in the case of two equal-sized particles due to the additional diffusion driving force provided by Ostwald ripening [10,11]. Lastly, the stability of these diffusion paths along defects, such as GBs, is typically associated with lower activation energies and higher diffusion rates. Consequently, the sintering of particles with misorientations forming GBs at the necks tends to be more effective [12–14]. Analytical relations of these factors have been proposed which have been shown to be effective in predicting the sintering state of various materials, such as Ag, Ni, and Cu [15,16].

The surface to volume ratios of the NPs (in the range of $10^9 \sim 10^6$ 1/m for particles diameter of 1 nm ~ 1 µm), such as the ones generated by laser ablation, are significantly higher than micro particles (in the range of $10^5 \sim 10^4$ 1/m for particles diameter of 10 µm ~ 100 µm). The sintering behavior of NPs is expected to be more significantly dominated by surface tension and surface diffusion. Therefore, the prior knowledge established on the effects of various factors on the sintering characteristics of micro particles may not be valid for NPs, even though some may be qualitatively similar [7,10,17–29]. For instance, NPs have higher fractions of under-coordinated surface atoms, which lowers their melting temperatures and significantly reduces the amount of energy input or time needed for them to reach sound fusion [7]. In fact, unlike the sintering of microparticles (e.g., powder metallurgy often requires hours of soaking at 70% of melting temperature and sometimes application of external pressure), NPs typically sinter within nanoseconds at the intended sintering temperatures which typically approach but are below the melting temperature.

Due to the transient nature of NPs sintering, studying it through experimental approaches alone can be challenging [30]. In contrast, molecular dynamics (MD), which can explicitly model atomic motion in pico-nano second scale, have proven effective in understanding NP sintering [7,18,31–37]. For instance, MD simulations have shown that the conventional sintering models' treatment of GBs as surface features of identical properties cannot be extrapolated to NPs, and that GBs' diffusion activation energies are strongly affected by their characteristics, including misorientation angles, planar orientation, curvature, etc. [24]. Therefore, for an accurate representation of the NP sintering, it is crucial that these attributes for the relevant physical processes to be properly accounted for [38]. Although the previous studies have laid the foundation knowledge regarding some sintering mechanisms and trends of NP sintering, quantitative relationships between sintering quality and various governing factors (such as the ones identified for micro particles as mentioned in the preceding text) are still lacking for metallic NPs.

This work attempts to quantify the role of several key influencing factors on the sintering of NPs using MD simulations. MD is uniquely suitable for this objective due to the characteristic time and length scales of the sintering process being in nanoseconds and nanometers, respectively. Pairs of contacting NPs of different sizes, materials, and orientations exposed to different sintering temperatures are simulated using MD. The effects of particle size, size ratio, tilt and twist grain boundaries, sintering temperature, and material type on the sintering quality in terms of neck size are investigated, quantified, and expressed in mathematical framework. *Section 2* describes the simulation procedure. In *Section 3*, simulation results, including sintering of equal-sized NPs (*Section 3.1*), unequal-sized NPs (*Section 3.2*), and equal-sized NPs with tilt and twist misorientation (*Section 3.3*), are presented. A predictive model is discussed in *Section 3.4*, and a summary and concluding remarks are included in *Section 4*.

2. Methodology

A laser-based single-step ANM technique has recently been developed to allow for the dry printing of a variety of materials, including Ag and Cu, on different substrates, like flexible polyimide [1,2]. This work used MD simulations to investigate the dependence of sintering effectiveness on various factors such as temperature, particle size, and material type. The findings can help guide fine-tuning the laser sintering parameters to achieve optimal final products. The MD simulations of the sintering process in this study follow the Stages (1-4) shown in **Figure 1**. NP doublets of identical materials of Ag and Cu were first equilibrated at ambient temperature (300 K) using a microcanonical ensemble (NVE). For the second Stage, the simulation temperature was regulated using a canonical ensemble (NVT). Subsequently, the NPs were heated individually to the desired sintering temperature in Stage 3 before being joined with each other at the inception of sintering. The total heating time was approximately 30 ps, which resulted in the heating rates being within a reasonable range of 10 K/ps to 30 K/ps [31]. To eliminate initial stresses, the initial smallest spacing between two NP surfaces at a specified temperature was selected as the equilibrium lattice parameter. The simulated sintering process lasted 5 ns.

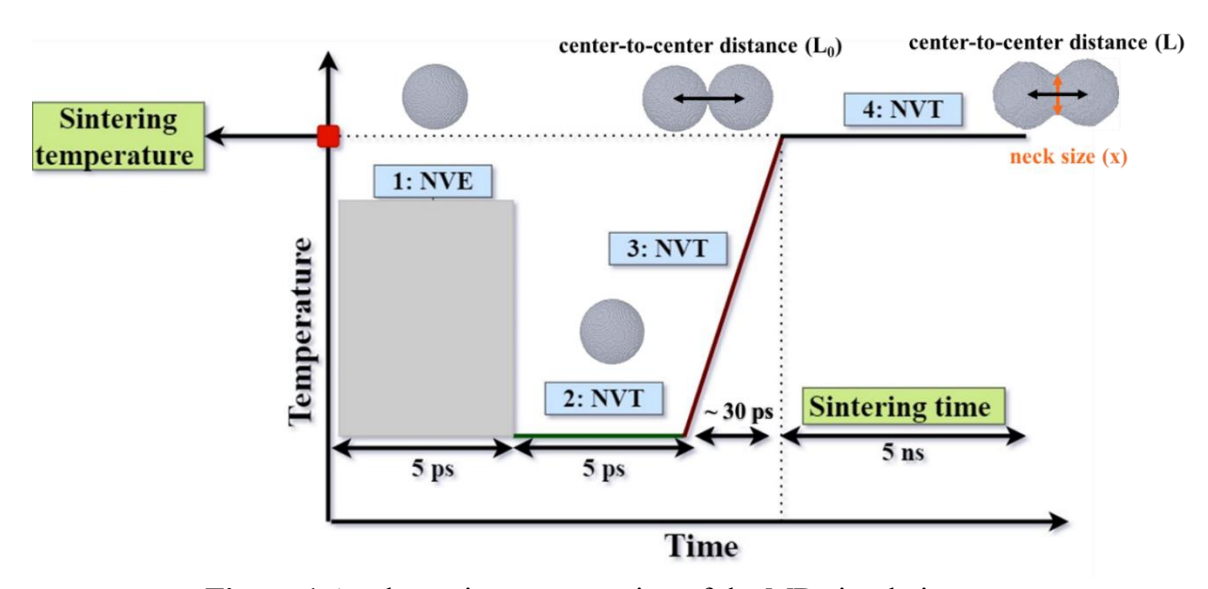


Figure 1 A schematic representation of the MD simulation steps.

The MD simulations performed with varying sizes, size ratios, temperatures, and misorientation angles for Ag and Cu NP doublets are summarized in **Table 1** and **Table 2**, respectively. The first column lists Ag and Cu as the selected materials. The second and third columns include the diameters of the two NPs. The NP doublets consisted of equal-sized and unequal-sized NPs. Particle sizes ranged from 5 to 25 nm. A series of equal-sized NP doublets, including 5 nm-5 nm, 10 nm-10 nm, 15 nm-15 nm, 20 nm-20 nm, and 25 nm-25 nm, were chosen to explore the effect of absolute size of NPs on sintering outcome. By keeping the size of one NP constant (i.e., at 15 nm), the effect of particle size ratio was investigated by varying the size of the other from 5 nm to 25 nm. The particle size ratios were expressed as the larger NP diameter to the smaller NP diameter. The doublets with the highest size ratios to the smallest size ratio were as follows: 15 nm-5 nm (3:1), 25 nm-15 nm (1.67:1), 15 nm-10 nm (1.5:1), and 20 nm-15 nm (1.4:1). The number of atoms ranged from several hundred to a few million.

The sintering temperatures were respectively chosen as 50, 60, and 70% of the bulk melting temperature of Ag ($T_m = 1234.95$ K) [39] and Cu ($T_m = 1358.15$ K) [40]. The bulk melting temperatures were chosen as references instead of the actual melting temperatures of the NPs, since the latter have strong dependence on the NPs' size. Using the NPs' melting temperatures would have coupled the effects of NP size and temperature. The misorientation angle was defined as the symmetric rotation of the two NPs in both tilt and twist, which forms tilt and twist grain boundaries between the NPs, respectively. Two symmetric tilted misorientation angles (θ) of 36.87° and 53.15° about the tilt axis of [100] were simulated since these angles were shown to have low-energy states and promote stable GBs [41,42] (see **Figure 2**). As for twist misorientations, since it is well known that pure twist GBs are inherently unstable and tend to spontaneously untwist, the identical two angles (i.e., 36.87° and 53.15°) were applied about the

[001] axis to examine their effect on sintering [43]. Each simulation is designated by the code of "Material_Diameters_Temperature_Tilt-Twist". Note that the second term enumerates the diameters of the two NPs in each doublet.

Nominally spherical Ag and Cu NPs were created with an FCC lattice and the [100], [010], and [001] crystallographic directions along the X-, Y-, and Z-axes, respectively (**Figure 2**). Each particle was illustrated by a circle with d diameter in equal-sized NPs. The large and small particles were represented by circles with D and d diameters in unequal-sized NPs, respectively. Several geometric parameters of a pair of particles, such as neck size (s), distance between sphere centers (L), dihedral angle (Ψ) , and neck radius of curvature (ρ) , change as sintering proceeded. A neck size (s) represented the narrowest connection between two NPs. Moreover, the distance between the sphere centers (L), which migrated toward one another during sintering, determined shrinkage. Although dihedral angle is typically defined for two intersecting planes, in the context of NP doublets, Ψ represents the angle between the tangential planes in the neck region as depicted in **Figure 2**. With a smaller dihedral angle, surface tension exerted a stronger driving force for sintering. The neck radius of curvature (ρ) is defined by the radius of the circle shown with dashed lines that best fits the neck surface curvature. A small value of ρ , is typically associated with a strong driving force for sintering.

The embedded atom method (EAM) interatomic potentials were used to describe the atomic interactions among Ag [44] and Cu [45] atoms. Cu-Ag cross species potential was not required, since the scope of work only concerned with only elementally pure NPs. For all simulations, shrink-wrapped boundary conditions were applied in three directions, and the time step was set to 5 fs, which has been shown to yield reliable results [46–48]. All the simulations in this study were performed using the Large-scale Atomic/Molecular Massively Parallel Simulator (LAMMPS), an

open source software distributed by Sandia National Laboratories [49]. Since no constraints were applied during simulations, rigid body translations and rotations often resulted from the initial contact between NPs [50]. The results were only analyzed after these motions were subtracted using Visual Molecular Dynamics (VMD) [51]. The configuration evolution of the coalescing NPs during sintering was analyzed with the Open Visualization Tool (OVITO) [52]. In order to understand the local lattice structural evolution throughout the sintering process, the polyhedral template matching method was used [53]. The green, red, and gray colors in the atomistic snapshots correspond to face-centered cubic (FCC), hexagonal closed packed (HCP), and other lattice structures, respectively.

Table 1 Diameters of Ag NPs, sintering temperatures, misorientation angles, and final designations used in this study.

Material	D1 (nm)	D2 (nm)	Sintering Temperature	Symmetric Tilt Angle,	Designation
	, ,		(K)	Twist Angle (°)	
Ag	5	5	864.465	0,0	$Ag_5-5_70\%T_m_0-0$
$\mathbf{A}\mathbf{g}$	5	5	740.97	0,0	$Ag_5-5_60\%T_{m_0}-0$
$\mathbf{A}\mathbf{g}$	5	5	617.475	0,0	$Ag_5-5_50\%T_{m}0-0$
$\mathbf{A}\mathbf{g}$	10	10	864.465	0,0	$Ag_10-10_70\%T_{m}_0-0$
$\mathbf{A}\mathbf{g}$	10	10	740.97	0,0	$Ag_10-10_60\%T_{m_0}-0$
$\mathbf{A}\mathbf{g}$	10	10	617.475	0,0	$Ag_10-10_50\%T_m_0-0$
$\mathbf{A}\mathbf{g}$	15	15	864.465	0,0	$Ag_15-15_70\%T_m_0-0$
$\mathbf{A}\mathbf{g}$	15	15	740.97	0,0	$Ag_15-15_60\%T_m_0-0$
$\mathbf{A}\mathbf{g}$	15	15	617.475	0,0	$Ag_15-15_50\%T_m_0-0$
$\mathbf{A}\mathbf{g}$	20	20	864.465	0,0	$Ag_20-20_70\%T_m_0-0$
$\mathbf{A}\mathbf{g}$	20	20	740.97	0,0	$Ag_20-20_60\%T_m_0-0$
$\mathbf{A}\mathbf{g}$	20	20	617.475	0,0	$Ag_20-20_50\%T_m_0-0$
$\mathbf{A}\mathbf{g}$	25	25	864.465	0,0	$Ag_25-25_70\%T_m_0-0$
$\mathbf{A}\mathbf{g}$	25	25	740.97	0,0	$Ag_25-25_60\%T_m_0-0$
$\mathbf{A}\mathbf{g}$	25	25	617.475	0,0	$Ag_25-25_50\%T_m_0-0$
Ag	15	5	864.465	0,0	Ag 15-5 70%T _m 0-0
$\mathbf{A}\mathbf{g}$	15	5	740.97	0,0	$Ag 15-5 60\%T_m 0-0$
$\mathbf{A}\mathbf{g}$	15	5	617.475	0,0	$Ag_{15-5}50\%T_{m}0-0$
$\mathbf{A}\mathbf{g}$	15	10	864.465	0,0	$Ag 15-10 70\%T_m 0-0$
$\mathbf{A}\mathbf{g}$	15	10	740.97	0,0	$Ag 15-10 60\%T_m 0-0$
$\mathbf{A}\mathbf{g}$	15	10	617.475	0,0	$Ag^{-}15-10^{-}50\%T_{m}^{-}0-0$
$\mathbf{A}\mathbf{g}$	15	20	864.465	0,0	$Ag^{-}15-20^{-}70\%T_{m}^{-}0-0$
$\mathbf{A}\mathbf{g}$	15	20	740.97	0,0	$Ag^{-}15-20^{-}60\%T_{m}^{-}0-0$
$\mathbf{A}\mathbf{g}$	15	20	617.475	0,0	$Ag^{-}15-20^{-}50\%T_{m}^{-}0-0$
$\mathbf{A}\mathbf{g}$	15	25	864.465	0,0	$Ag^{-}15-25^{-}70\%T_{m}^{-}0-0$
$\mathbf{A}\mathbf{g}$	15	25	740.97	0,0	$Ag_{15-25}60\%T_{m}0-0$
$\mathbf{A}\mathbf{g}$	15	25	617.475	0,0	$Ag 15-25 50\%T_m 0-0$
Ag	15	15	864.465	36.87,0	Ag 15-15 70%T _m 36-0
$\mathbf{A}\mathbf{g}$	15	15	740.97	36.87,0	$Ag^{-}15-15^{-}60\%T_{m}^{-}36-0$
$\mathbf{A}\mathbf{g}$	15	15	617.475	36.87,0	$Ag^{-}15-15^{-}50\%T_{m}^{-}36-0$
$\mathbf{A}\mathbf{g}$	15	15	864.465	53.15,0	$Ag^{-}15-15^{-}70\%T_{m}^{-}53-0$
$\mathbf{A}\mathbf{g}$	15	15	740.97	53.15,0	$Ag^{-}15-15^{-}60\%T_{m}^{-}53-0$
$\mathbf{A}\mathbf{g}$	15	15	617.475	53.15,0	$Ag^{-}15-15^{-}50\%T_{m}^{-}53-0$
$\mathbf{A}\mathbf{g}$	15	15	864.465	0,36.87	$Ag_{15-15}^{-}70\%T_{m}^{-}0-36$
$\mathbf{A}\mathbf{g}$	15	15	740.97	0,36.87	$Ag^{-}15-15^{-}60\%T_{m}^{-}0-36$
$\mathbf{A}\mathbf{g}$	15	15	617.475	0,36.87	$Ag^{-}15-15^{-}50\%T_{m}^{-}0-36$
$\mathbf{A}\mathbf{g}$	15	15	864.465	0,53.15	$Ag^{-}15-15^{-}70\%T_{m}^{-}0-53$
$\mathbf{A}\mathbf{g}$	15	15	740.97	0,53.15	$Ag^{-}15-15^{-}60\%T_{m}^{-}0-53$
$\mathbf{A}\mathbf{g}$	15	15	617.475	0,53.15	$Ag^{-15-15} 50\%T_m 0-53$

Table 2 Diameters of Cu NPs, sintering temperatures, misorientation angles, and final designations used in this study.

Material	D1	D2	Sintering	Symmetric	Designation
	(nm)	(nm)	Temperature	Tilt Angle,	5
			(K)	Twist Angle (°)	
Cu	5	5	950.705	0,0	$Cu_5-5_70\%T_{m_0}-0$
Cu	5	5	814.89	0,0	$Cu_5-5_60\%T_{m_0}0-0$
Cu	5	5	679.075	0,0	$Cu_5-5_50\%T_{m_0}0-0$
Cu	10	10	950.705	0,0	$Cu_10-10_70\%T_{m_0}-0$
Cu	10	10	814.89	0,0	$Cu_10-10_60\%T_{m_0}-0$
Cu	10	10	679.075	0,0	$Cu_10-10_50\%T_{m_0}0-0$
Cu	15	15	950.705	0,0	$Cu_15-15_70\%T_{m_0}-0$
Cu	15	15	814.89	0,0	$Cu_15-15_60\%T_{m_0}-0$
Cu	15	15	679.075	0,0	$Cu_15-15_50\%T_{m_0}-0$
Cu	20	20	950.705	0,0	$Cu_20-20_70\%T_{m_0}0-0$
Cu	20	20	814.89	0,0	$Cu_20-20_60\%T_{m_0}0-0$
Cu	20	20	679.075	0,0	$Cu_20-20_50\%T_{m_0}0-0$
Cu	25	25	950.705	0,0	$Cu_25-25_70\%T_{m_0}0-0$
Cu	25	25	814.89	0,0	$Cu_25-25_60\%T_{m_0}0-0$
Cu	25	25	679.075	0,0	$Cu_25-25_50\%T_m_0-0$
Cu	15	5	950.705	0,0	$Cu_15-5_70\%T_m_0-0$
Cu	15	5	814.89	0,0	$Cu_15-5_60\%T_m_0-0$
Cu	15	5	679.075	0,0	$Cu_15-5_50\%T_m_0-0$
Cu	15	10	950.705	0,0	$Cu_15-10_70\%T_{m_0}-0$
Cu	15	10	814.89	0,0	$Cu_15-10_60\%T_{m_0}-0$
Cu	15	10	679.075	0,0	$Cu_15-10_50\%T_{m_0}0-0$
Cu	15	20	950.705	0,0	$Cu_15-20_70\%T_{m_0}0-0$
Cu	15	20	814.89	0,0	$Cu_15-20_60\%T_m_0-0$
Cu	15	20	679.075	0,0	$Cu_15-20_50\%T_{m_0}0-0$
Cu	15	25	950.705	0,0	$Cu_15-25_70\%T_{m_0}0-0$
Cu	15	25	814.89	0,0	$Cu_15-25_60\%T_{m_0}0-0$
Cu	15	25	679.075	0,0	$Cu_15-25_50\%T_{m_0}0-0$
Cu	15	15	950.705	36.87,0	$Cu_15-15_70\%T_{m_3}6-0$
Cu	15	15	814.89	36.87,0	$Cu_15-15_60\%T_{m_3}6-0$
Cu	15	15	679.075	36.87,0	$Cu_15-15_50\%T_{m_3}6-0$
Cu	15	15	950.705	53.15,0	$Cu_15-15_70\%T_{m_53-0}$
Cu	15	15	814.89	53.15,0	$Cu_15-15_60\%T_{m_5}3-0$
Cu	15	15	679.075	53.15,0	$Cu_15-15_50\%T_{m_5}3-0$
Cu	15	15	950.705	0,36.87	$Cu_15-15_70\%T_{m_0}-36$
Cu	15	15	814.89	0,36.87	$Cu_15-15_60\%T_m_0-36$
Cu	15	15	679.075	0,36.87	$Cu_15-15_50\%T_m_0-36$
Cu	15	15	950.705	0,53.15	$Cu_15-15_70\%T_{m_0}-53$
Cu	15	15	814.89	0,53.15	$Cu_15-15_60\%T_m_0-53$
Cu	15	15	679.075	0,53.15	$Cu_15-15_50\%T_{m_0}-53$

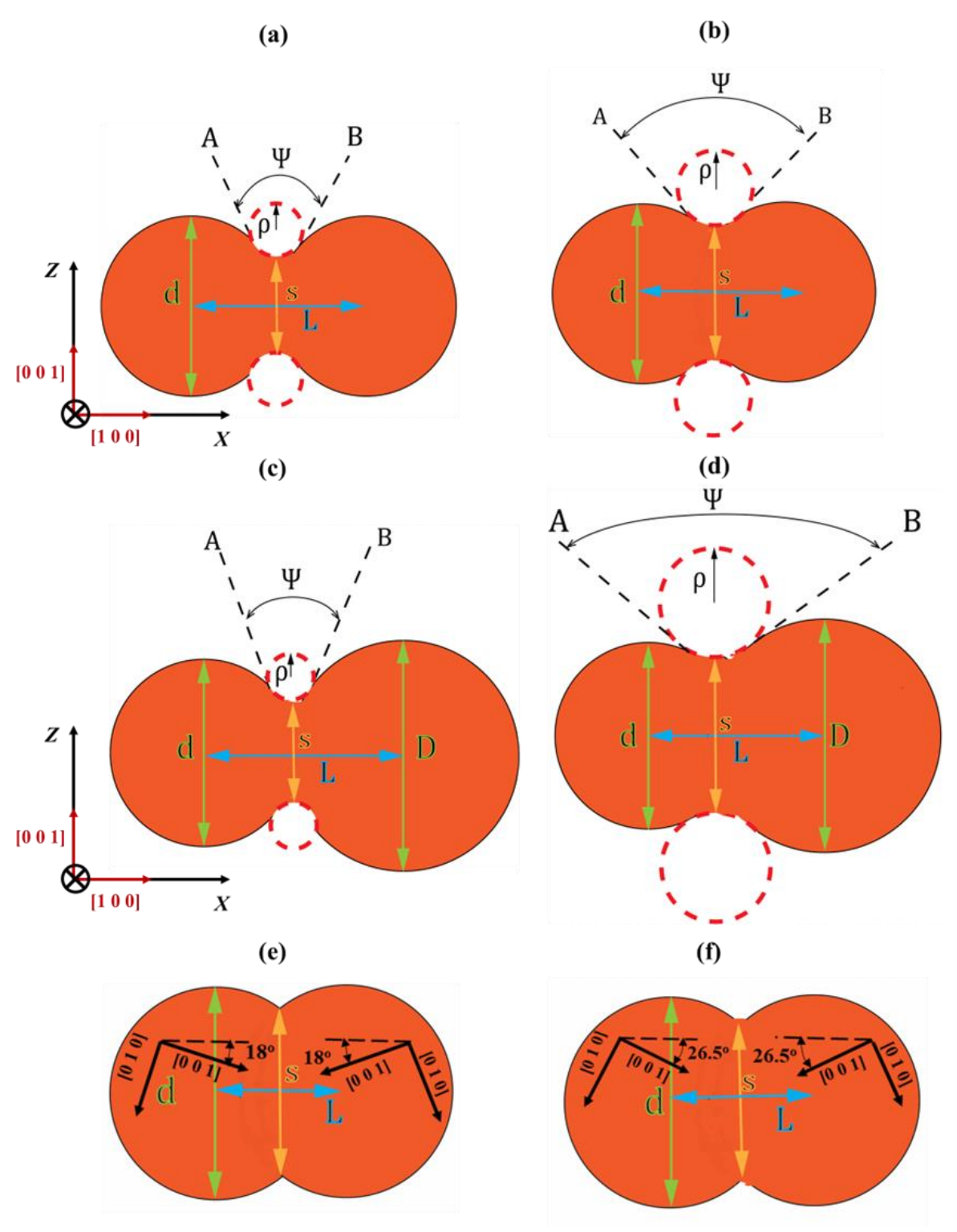


Figure 2 Schematic illustrations of sintering states for (a,b) equal-sized NPs at early and later stages, (c,d) unequal-sized NPs at early and later stages, and (e,f) equal-sized NPs with two symmetric tilted misorientation angles of 36.87° and 53.15° about the tilt axis of [100] at a later stage. The crystallographic directions of the NPs without tilts and twists are provided with respect to the coordinate system.

3. Results and discussion

This section proceeds by presenting the MD simulated sintering behavior of NPs in the following order: Section 3.1 equal-sized NPs, Section 3.2 unequal-sized NPs, and Section 3.3 equal-sized NPs with tilt and twist misorientation. Although multiple parameters, such as the distance between two NPs (*L*) (see **Figure 2**), could be used to describe the sintering state of particles, the neck size (*s*) was adopted in this work since it was calculated with ease from the XYZ data outputs of MD simulations. In addition, selected NP doublets in the sintered state are also visualized and presented in each section to reveal the potential influence of size, sintering temperature, and material on their morphologies. The changes in neck size during sintering and the crystal structures during sintering for equal-sized, unequal-sized, and equal-sized tilted and twisted NPs are discussed in Sections 3.1, 3.2, and 3.3, respectively. Finally, based on the neck size data presented, Section 3.4 proposes a model to predict the characteristic sintering times based on the particle size, temperature, and material type.

3.1 Sintering behavior of equal-sized NPs

The final morphologies of equal-sized NPs with diameters of 5 nm and 15 nm at different sintering temperatures by the end of the simulated time of 5 ns are compared in **Figure 3(a)-(d)**. Crystallographic facets appeared in the smallest NP's final morphology at the highest sintering temperature (see the bottom of **Figure 3(a)**). These facets belonged to low index crystallographic planes (such as {100}, {110}, and {111}), had low surface energies, and tended to form for smaller particles and at elevated temperatures due to the shorter diffusion pathways and higher diffusion coefficients [54]. Since the simulated duration for all simulations were the same, a narrower neck region or smaller dihedral angle at the neck shown in the figure indicated a less effective sintering process. For instance, at every temperature, the smaller NPs exhibited final morphologies with

better-developed neck regions, along with larger dihedral angles and neck radii (relative to the particle diameter) than larger NPs, indicating more effective sintering (compare the bottom of **Figure 3(c)** with the bottom of **Figure 3(a)**). Smaller NPs had more effective sintering, due to the shorter diffusion paths, and the more influential presence of surface diffusion, which was more effective than volumetric diffusion.

For NPs with a given diameter, the sintering process was more effective at a higher temperature (compare the bottom of Figure 3(a) with the middle of Figure 3(a)) and (compare the bottom of Figure 3(b) with the middle of Figure 3(b)). This was attributed to the increased mobility of atoms driven by elevated thermal energy, facilitating their migration to the neck region. In addition, compared to Cu NPs, Ag NPs sintered more effective at all temperatures (see the bottom of Figure 3(c) and Figure 3(d)). This was because its cohesive energy (-2.85 eV) [55] was significantly smaller than that of Cu (-3.54 eV) [55,56], which made Ag atoms having higher mobility than Cu at any given temperature, thus facilitating further diffusion and sintering [57]. Moreover, due to lower stacking fault energy of Ag, nanotwins and stacking faults appeared, especially when the particle size was small (see the middle of Figure 3(c) and Figure 3(d)). This was likely due to discrete deformation events, such as slip or twinning, driven by the minimization surface energy, which for small NPs was more influential.

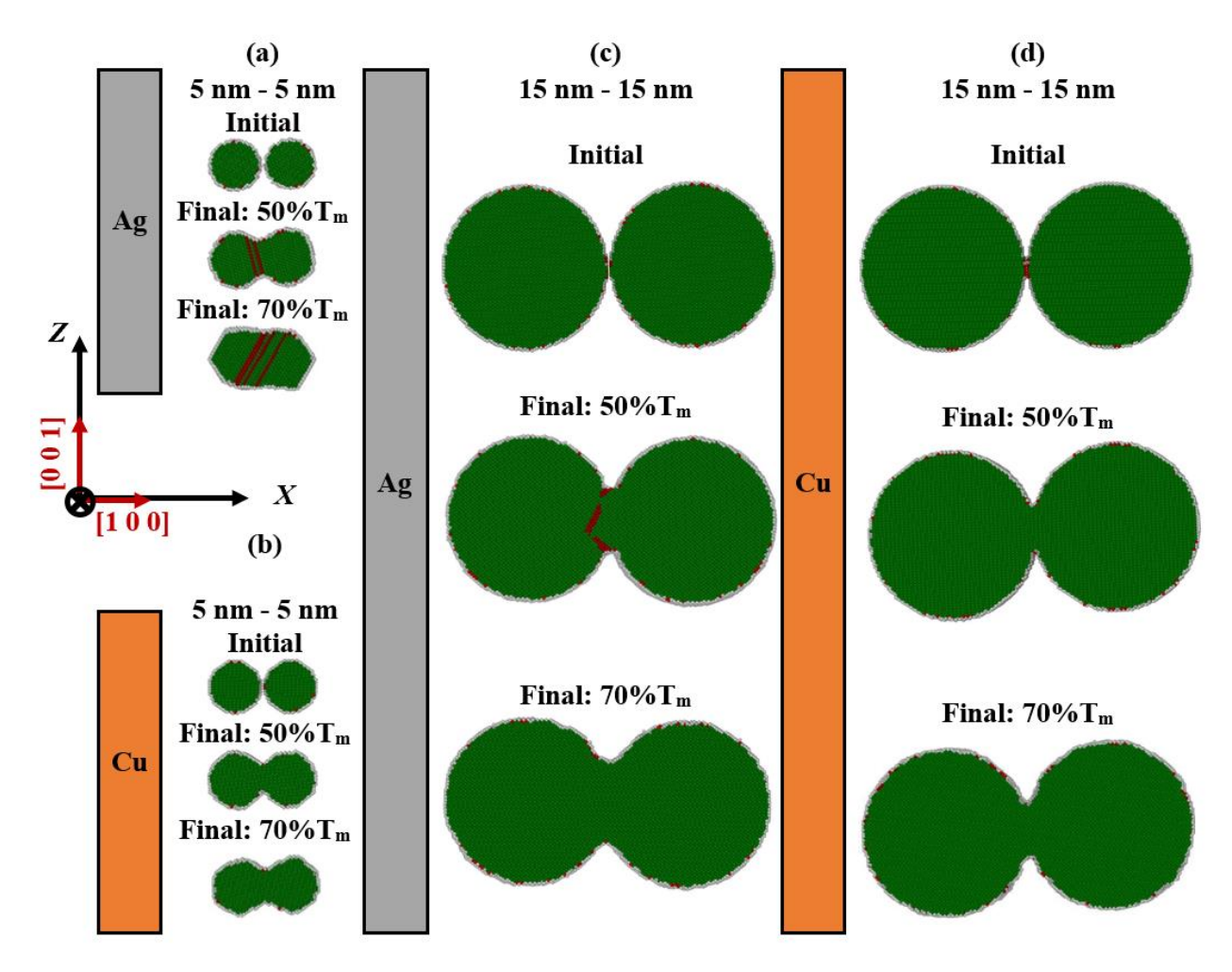


Figure 3 Examples of the resulting morphologies of equal-sized NPs at $50\%T_m$ and $70\%T_m$ sintering temperatures: (a) Ag NPs with a diameter of 5 nm, (b) Cu NPs with a diameter of 5 nm, (c) Ag NPs with a diameter of 15 nm, and (d) Cu NPs with a diameter of 15 nm. The crystallographic directions of the NPs are provided with respect to the coordinate system.

The changes in normalized neck size with respect to time for equal-sized Ag and Cu NPs for all simulated temperatures and diameters are shown in **Figure 4(a)-(b)**. The observed steps in some curves (e.g., see Ag_5-5_70%T_m_0-0 in **Figure 4(a)**, and Cu_5-5_70%T_m_0-0 in **Figure4(b)**), was ascribed to discrete events discussed previously, encompassing the movement and interaction of defects (see **Figure 4(a)**). The neck size was normalized by the equivalent diameter (D_{eq}), which for equal-sized NPs, equaled the diameter of each NP. To calculate the neck size, the atoms near the neck region between two NPs were sliced successively into several thin

segments perpendicular to the doublet's common axis (i.e., the *x*-axis shown in **Figure 2**) at each time step. On each slice, the largest distance between any two atoms was calculated, and the slice whose distance value was the smallest was selected as the neck. On the neck slice, the aforementioned maximum distance was defined as neck size (*s*).

From **Figure 4**, it is evident that all sintering processes began with an initial stage where the neck size rapidly grows. This was followed by a more gradual change of neck size. In the initial stage, the bonding between NPs was mainly due to mechanical interaction, and the growth of the neck is relatively temperature-independent [47]. As the particles adhered to one another, their overall surface area decreased. Furthermore, the particles underwent a combination of elastic [58] and plastic deformations as they bonded together and neck grew. Nevertheless, after the initial mechanical contact (the initial portions of the curves in **Figure 4** with larger slopes), the sintering process was predominantly governed by diffusion, which was expedited by elevated temperatures, facilitating the migration of atoms from the particles to the neck region. Treating diffusion as a reaction, its rate was described by the Arrhenius relation [59]:

$$J = J_0 \exp^{-\frac{E_a}{kT}} \tag{1}$$

where J is the reaction rate per unit time, E_a is the diffusion activation energy. The Boltzmann constant, denoted as k, when multiplied the temperature (T) in the denominator of the base value of the exponential function, signifies the role of thermal energy of atoms. Moreover, the pre-exponential factor J_0 represents the attempt frequency of diffusion per atom and is related to the Debye frequency. Note that although Eq. 1 adopts the same basic form as the equation for diffusion coefficients, it is not to be confused with the latter. Rather, it is used to illustrate the effects of temperature on the diffusion rate measured by the frequency of atomic diffusion events (with the

unit of volume per unit time). Corresponding Cu's higher cohesive energy than Ag, the diffusion activation energy of Cu was also greater than Ag [59,60] and Cu's diffusion rate was lower than Ag at a given temperature. Therefore, sintering was more effective for Ag NPs than Cu NPs, as indicated by the overall higher values of s/D_{eq} at the end of the simulation.

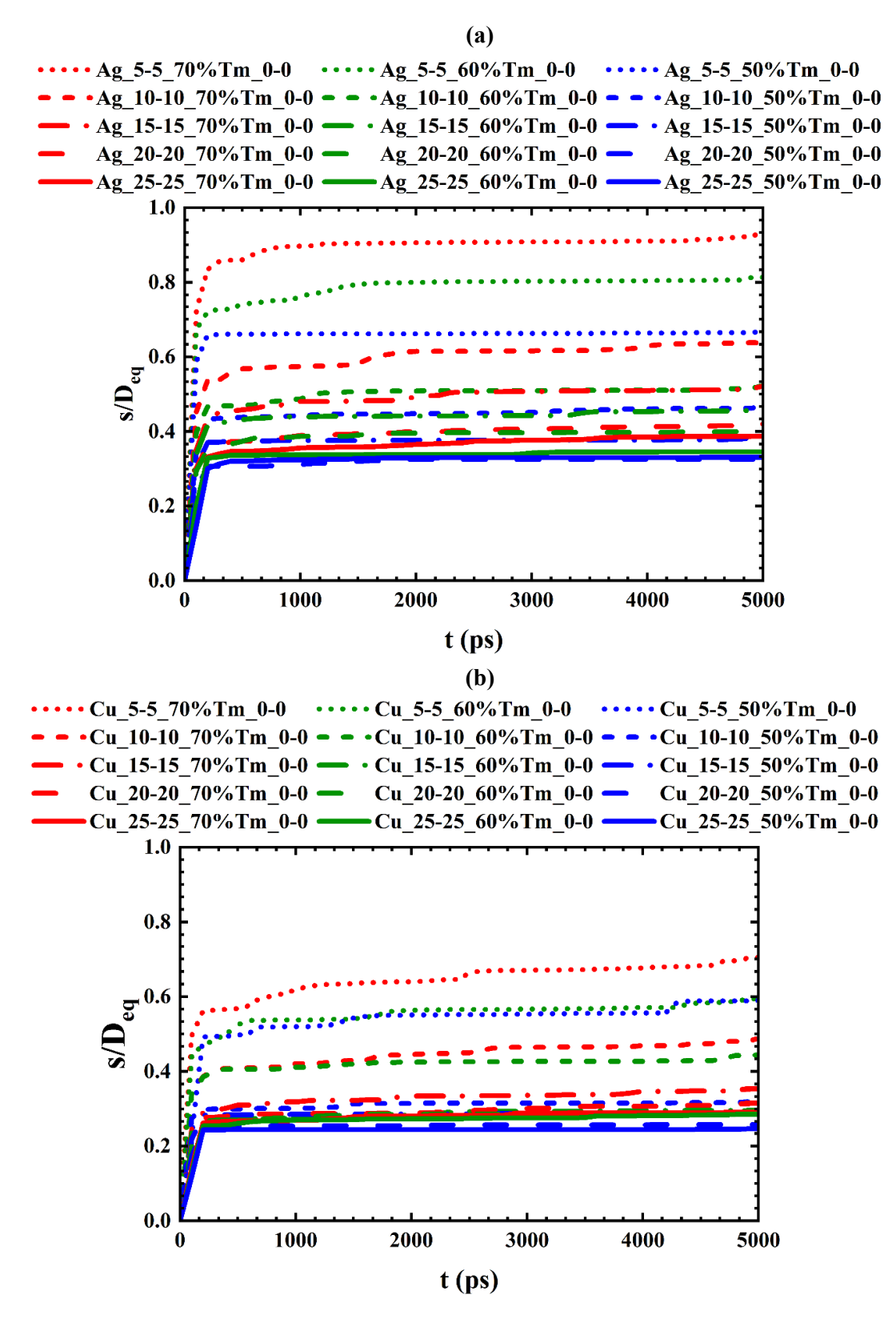


Figure 4 Normalized neck size of equal-sized (a) Ag NPs and (b) Cu NPs with distinct absolute sizes at different temperatures as functions of time.

3.2 Sintering behavior of unequal-sized NPs

A comparison of the initial and sintered morphologies of selected unequal-sized NP doublets, including those with diameters of 5 nm and 15 nm, as well as 15 nm and 25 nm at different sintering temperatures is shown in **Figure 5(a)-(d)**. For the simplicity of analysis, an equivalent diameter was used to capture the sintering behavior of unequal-sized NP doublets and compared with the examples of equal-sized NPs. The equivalent diameter (D_{eq}) should be such that the initial conditions of the sintering, such as the dihedral angle, for the unequal-sized NP doublet were similar to a doublet of equal-sized NP with size D_{eq} . A reasonable measure of the equivalent diameter had been suggested by Yang et al. [22] as:

$$D_{eq} = \frac{2 D \times d}{D + d} \tag{2}$$

where *d* and *D*, are the diameters of the smaller and larger NPs, respectively. There were some discernable similarities between the sintering of equal-sized NPs and unequal-sized NPs, since the majority of both sintering processes was still controlled by diffusion. The observed NP morphologies substantiated these similarities, and the existing trends occurred for the same reason discussed extensively in *Section 3.1*. For example, sintering was more effective at higher temperatures (compare the middle of **Figure 5(d)** and the bottom of **Figure 5(d)**), smaller equivalent diameter (compare the middle of **Figure 5(a)** and **Figure 5(b)**). Moreover, there were some facets formed in case of Ag_15-5_70%Tm_0-0 (see the bottom of **Figure 5(a)**), similar to the observations made in *Section 3.1*. Finally, the stacking fault only appeared in Ag NPs than in Cu NPs, due to Ag's lower stacking fault energy than Cu [61] (see the middle of **Figure 5(a)**).

The sintering behavior of unequal-sized NPs nevertheless differed from equal-sized NPs in some other aspects due to the difference in the surface tension-induced pressure between two NPs. Pressure across a curved surface was directly proportional to the surface tension and inversely proportional to surface radius of curvature. In the context of unequal-sized NPs, the smaller one had smaller radius of curvature and hence experiences a higher pressure than larger NP. This pressure difference caused the Ostwald ripening phenomenon, in which atoms tended to diffuse from regions of higher pressure (i.e., the smaller NP) to regions of lower pressure (i.e., the larger NP), see the bottom of **Figure 5(a)**. This was especially evident in the bottom panel of **Figure 5(a)** for the case of Ag_15-5_70%T_{m_0}-0, where the smaller Ag particle is partially absorbed by the larger one. This implied that both the particle size ratios (i.e., Larger NP: Smaller NP) and the absolute size of each NP affected the sintering effectiveness.

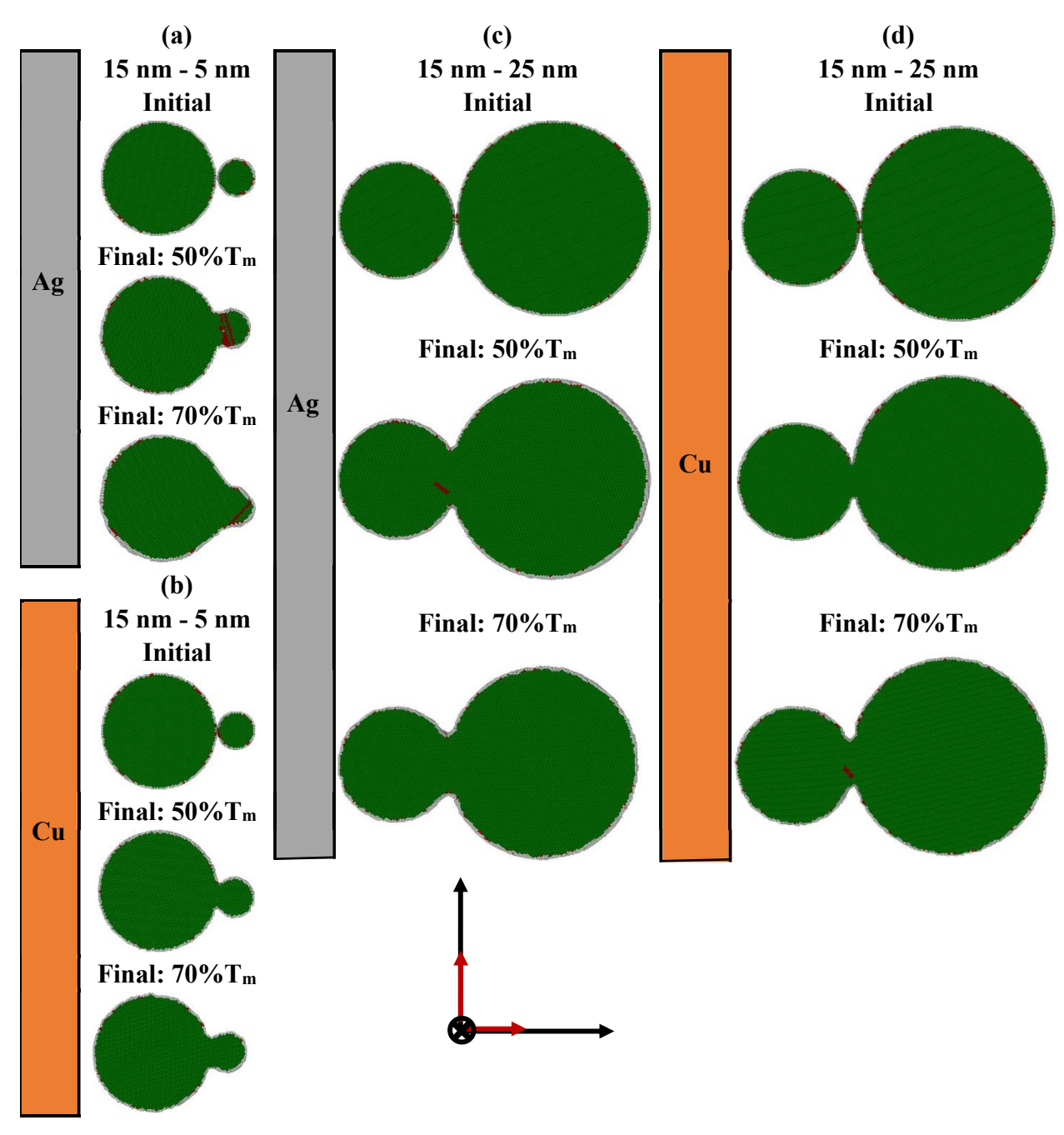


Figure 5 Examples of the resulting morphologies of unequal-sized NPs at 50%T_m and 70%T_m sintering temperatures: (a) Ag NPs with diameters of 15 nm and 5 nm, (b) Cu NPs with diameters of 15 nm and 5 nm, (c) Ag NPs with diameters of 15 nm and 25 nm, and (d) Cu NPs with diameters of 15 nm and 25 nm. The crystallographic directions of the NPs are provided with respect to the coordinate system.

The changes in normalized neck size values with respect to time of unequal-sized NPs at various temperatures and diameters are shown in **Figure 6**. The values of sintering effectiveness(e.g., more effective sintering would result in a larger normalized neck size by the end of a simulation) were consistent with the observations related to the morphologies of unequal-sized NPs, specifically higher temperatures and Ag NPs than Cu NPs led to more effective sintering. Furthermore, the doublet of NPs with diameters of 5 nm and 15 nm exhibited the most effective sintering among the all studied cases. Similar to the sintering of equal-sized NPs, all the curves shown in the figure had a change in the slope after a short time, suggesting a transition from two different sintering mechanisms: elastic and plastic-based sintering to diffusion-based sintering.

When studying the changes in the sintering of unequally-sized NPs, it was imperative to not solely rely on the equivalent diameter, but also took into account the effect of particle size ratio. At each temperature, the sintering effectiveness increased by increasing the particle size ratio when the larger NP was the same (compare Ag_15-5_70%T_m_0-0 and Ag_15-10_70%T_m_0-0 in Figure 6(a)). However, when the small NP size remained constant, but the size ratio increased, the sintering effectiveness of particle doublets did not necessarily increase (compare Ag_15-20_70%T_m_0-0 and Ag_15-25_70%T_m_0-0 in Figure 6(a)). This is due to the fact that, whereas bigger particle size ratios normally favored sintering, the increase in equivalent diameter may counteracted this effect. As a result, both the equivalent diameter and the particle size ratio must be considered in order to comprehend their combined influence on sintering. A careful comparison between Figures 4 and 6 reveals that the sintering effectiveness of unequal-sized NPs at a specific temperature appeared to always lie between the that of cases for equal-sized NPs of the respective sizes. For example, the curve for Ag_15-5_70%T_m_0-0 in Figure 6 falls between the curves for

Ag_5-5_70%T_m_0-0 and Ag_15-15_70%T_m_0-0 in **Figure 4** (the vertical axes of the figures have the same scale for ease of comparison).

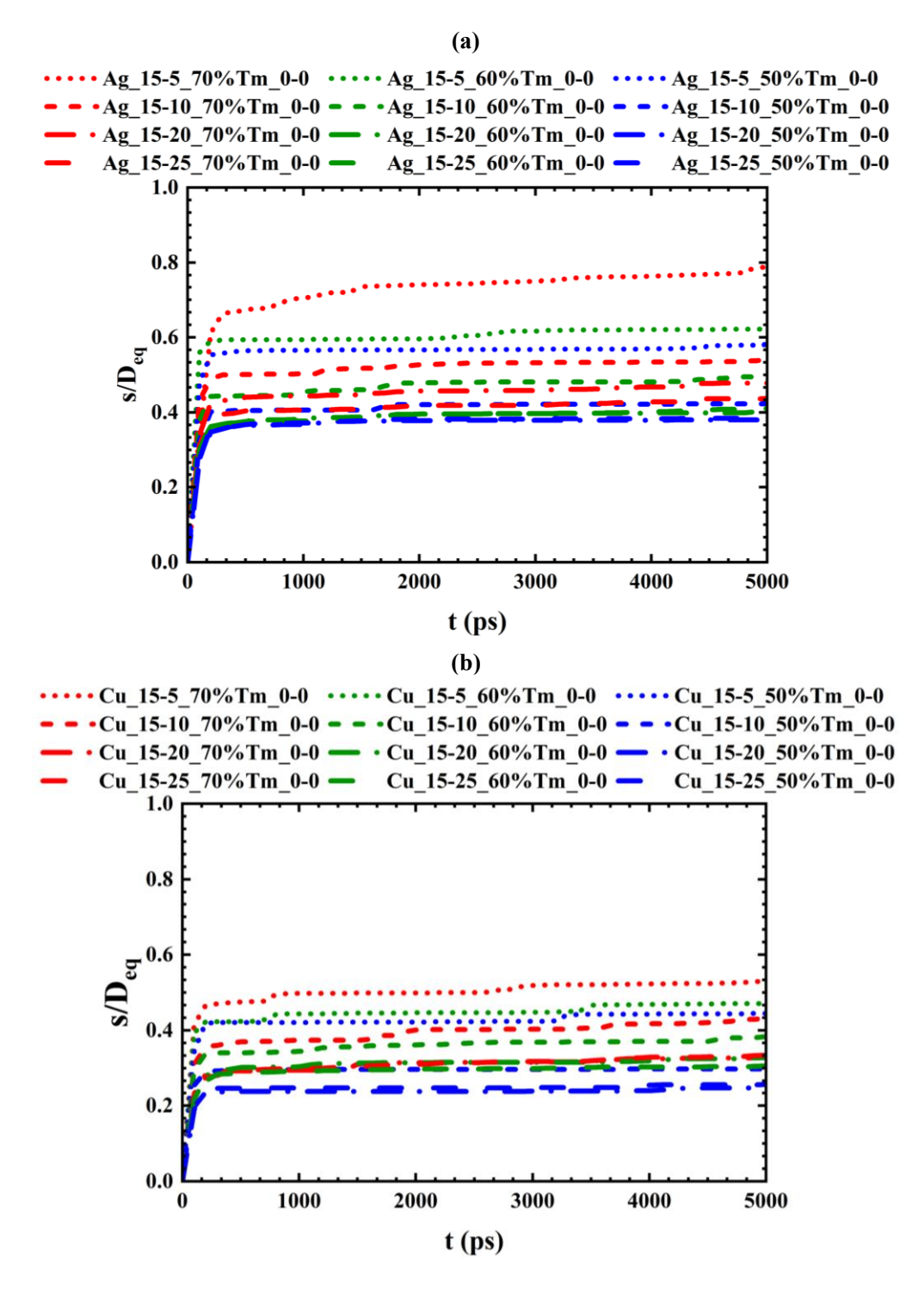


Figure 6 Normalized neck size values of unequal-sized (a) Ag NPs and (b) Cu NPs with distinct size ratios at different temperatures as functions of time.

3.3 Sintering behavior of equal-sized NPs with tilt and twist misorientations

A comparison of the final morphologies of Ag NPs and Cu NPs at different temperatures and two different symmetric tilted misorientation angles are shown in Figure 7(a)-(d). It is evident from the figure that the overall effect of temperature observed from the previous sections, i.e., higher temperature corresponds to more effective sintering, are still valid. The crystallographic misorientation of the adjacent NPs formed GBs between the two NPs, which were visualized in red color. The atoms were colored based on to the local lattice environment according to the polyhedral template matching method. More or less red atoms visualized at the GBs indicated the higher or lower degree of atomic disordering which is often indicative of higher or lower diffusion coefficients, respectively. At the highest simulated sintering temperature, the GB formed with the symmetric tilted misorientation angle of 36.87° resulted in the most atomic disordering. Indeed, the sintering under this condition appeared to be the most complete. In comparison, the larger GB indicated that the GBs formed with the symmetric tilted misorientation angle of 53.15°, which were much more ordered and corresponded to less effective sintering (compare the bottom of Figure 7(a) and the bottom of Figure 7(b), also compare the bottom of Figure 7(c) and the bottom of Figure 7(d)).

Changes in normalized neck size values of tilted NPs with respect to time at various temperatures and misorientation angles are shown in **Figure 8**. Comparing **Figures 4** and **8**, tilted NPs had a more effective sintering than NPs without misorientation angles, indicating that the formation of a GB facilitated atom diffusion. Moreover, it was evident that temperature change had a more significant effect on the sintering of tilted NPs compared to cases without misorientation angles (compare Ag_15-15_50%T_m_0-0 and Ag_15-15_70%T_m_0-0 in **Figure 4(a)** to Ag 15-15_50%T_m 36-0 and Ag 15-15_70%T_m 36-0 in **Figure 8(a)**). This was because

the diffusion of tilted Ag NPs was dominated by GBs which had lower diffusion activation energies than Ag NPs that were not misoriented. Therefore, the lower activation energies made their diffusion rates more susceptible to temperature variations (see Eq. 1). For the same reason, tilted Ag NPs' lower diffusion activation energy compared to tilted Cu NPs, made them more susceptible to temperature changes (compare Ag_15-15_50%T_m_36-0 and Ag_15-15_70%T_m_36-0 in Figure 8(a) to Cu_15-15_50%T_m_36-0 and Cu_15-15_70%T_m_36-0 in Figure 8(b)).

The final morphologies of Ag NPs and Cu NPs with twist misorientations at the lowest sintering temperature and the highest symmetric twisted angle are presented in Figure 9. During the early stages of sintering, a GB formed in the twisted NPs similar to tilted NPs. However, the screw dislocations within the twist GB were glissile and could repel each other, which in effect untwisted the NPs and the GBs disappeared shortly after (see the top of Figure 9(a) and Figure 9(b)). The changes in normalized neck size values of twisted NPs with respect to time at various temperatures and twisted misorientation angles are shown in Figure 10. Similar to the tilted NPs, sintering was more effective for a twist misorientation angle of 36.87° compared to a twist misorientation angle of 53.15° indicating that the GBs with higher twist angle had more atomic disorder which favored further diffusion. Compared to equal-sized NPs with the same diameters, the sintering was more effective for twisted equal-sized NPs (e.g., see Ag 15-15 60%T_m 0-36 and Ag 15-15 60%T_m 0-53 vs. Ag 15-15 60%T_m 0-0 in Figure 10(a)). This indicated that although the formed GBs between twisted NPs were temporary, they still facilitated sintering. The sintering was more effective for tilted NPs than twisted NPs, since the GB formed in the tilted NPs was stable and was available during the whole sintering process (compare Ag 15-15 70%T_m 36-0 in Figure 8(a) and Ag 15-15 70%T_m 0-36 in Figure 10(a), and compare Cu 15-15 60%T_m 36-0 in Figure 8(b) and Cu 15-15 60%T_m 0-36 in Figure 10(b)). The sintering of twisted Ag NPs was more susceptible to temperature change than Cu NPs due to their corresponding smaller values of activation energy for diffusion, as explained earlier (compare $Ag_5-5_70\%T_m_0-36$ vs. $Ag_5-5_50\%T_m_0-36$ in **Figure 10(a)**, and $Cu_5-5_70\%T_m_0-36$ vs. $Cu_5-5_50\%T_m_0-36$ in **Figure 10(b)**).

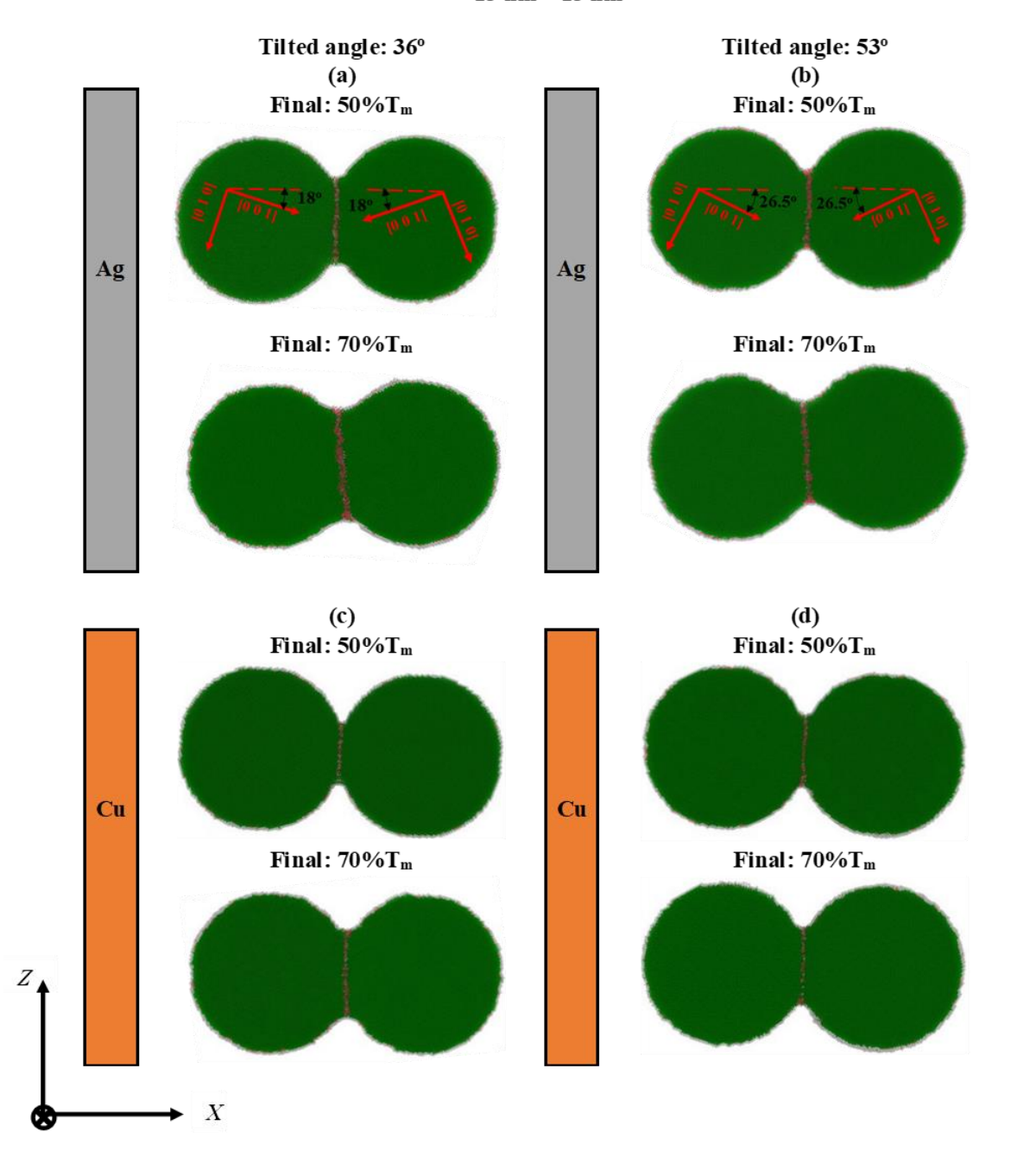
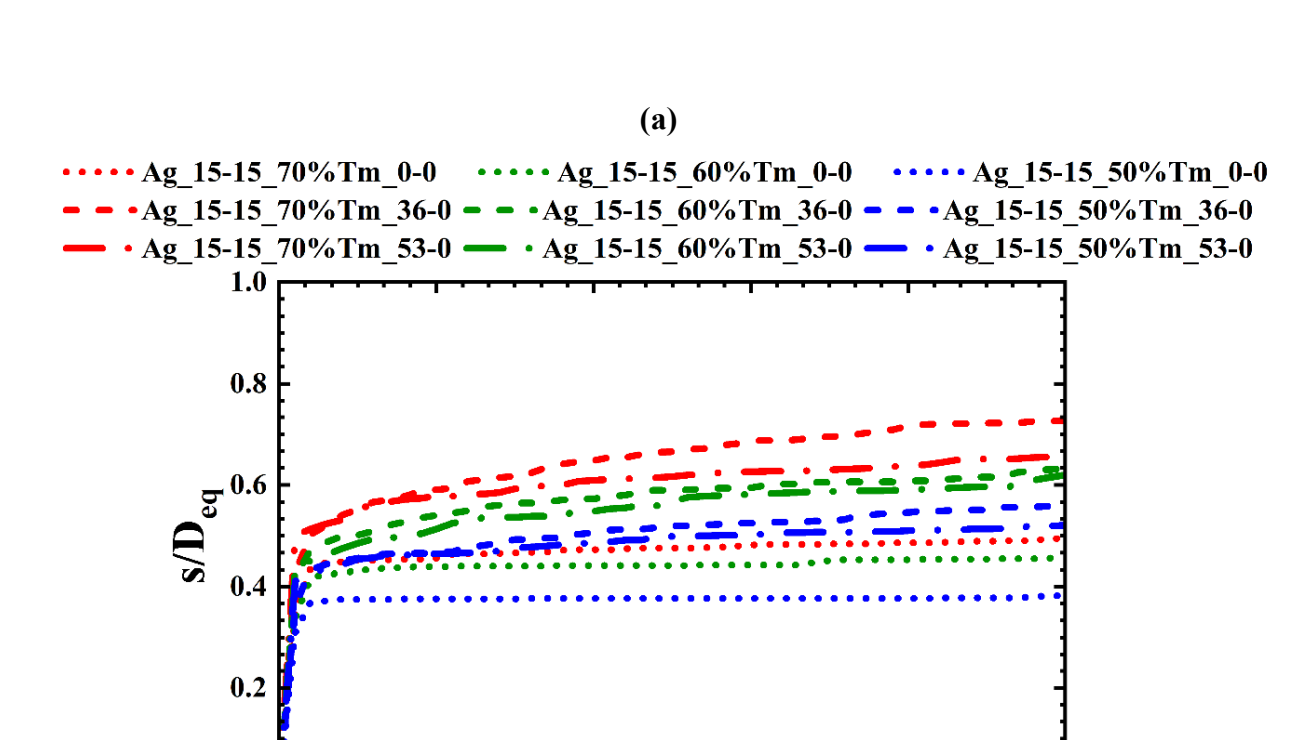


Figure 7 Examples of the resulting morphologies of equal-sized tilted NPs with a diameter of 15 nm at 50%T_m and 70%T_m sintering temperatures: (a) Ag NPs with a tilted misorientation angle of 36.87°, (b) Ag NPs with a tilted misorientation angle of 53.15°, (c) Cu NPs with a tilted misorientation angle of 53.15°.



t (ps)

0.0

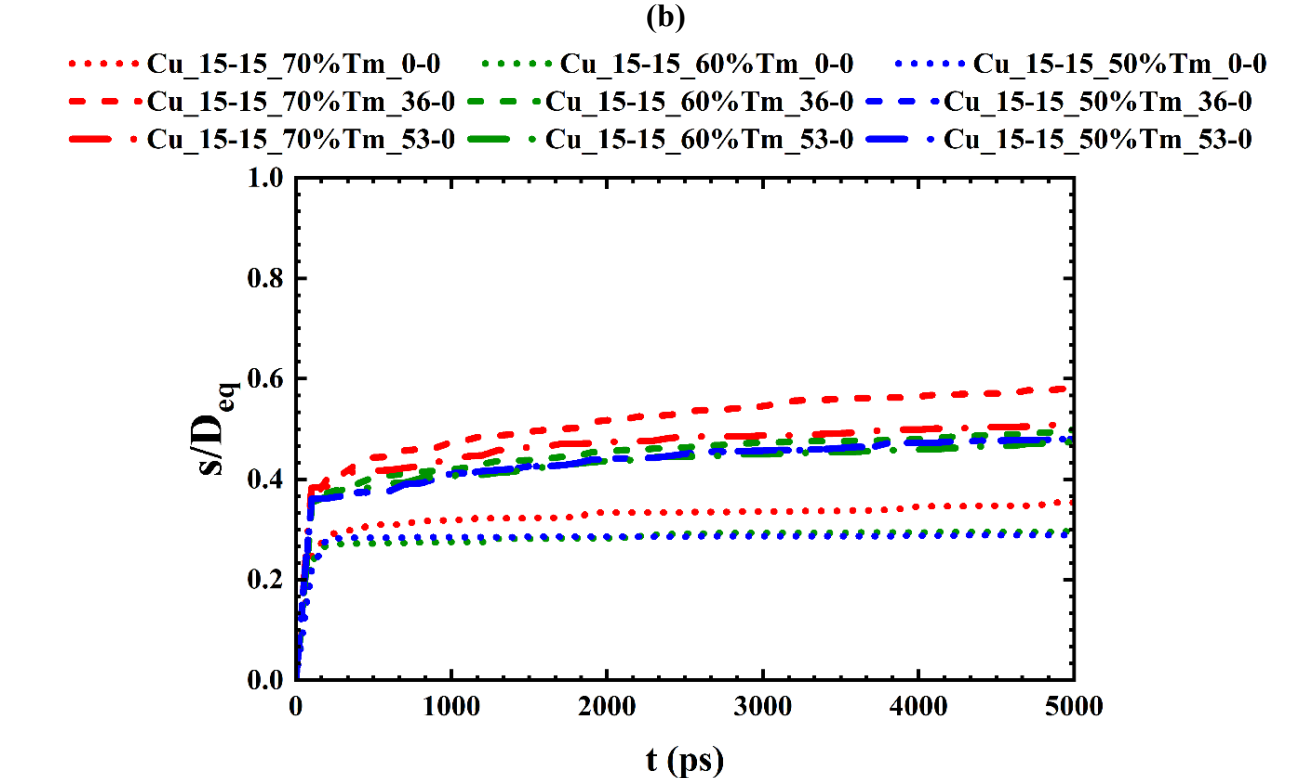


Figure 8 Normalized neck size values of tilted (a) Ag NPs and (b) Cu NPs with various misorientation angles at different temperatures as functions of time.

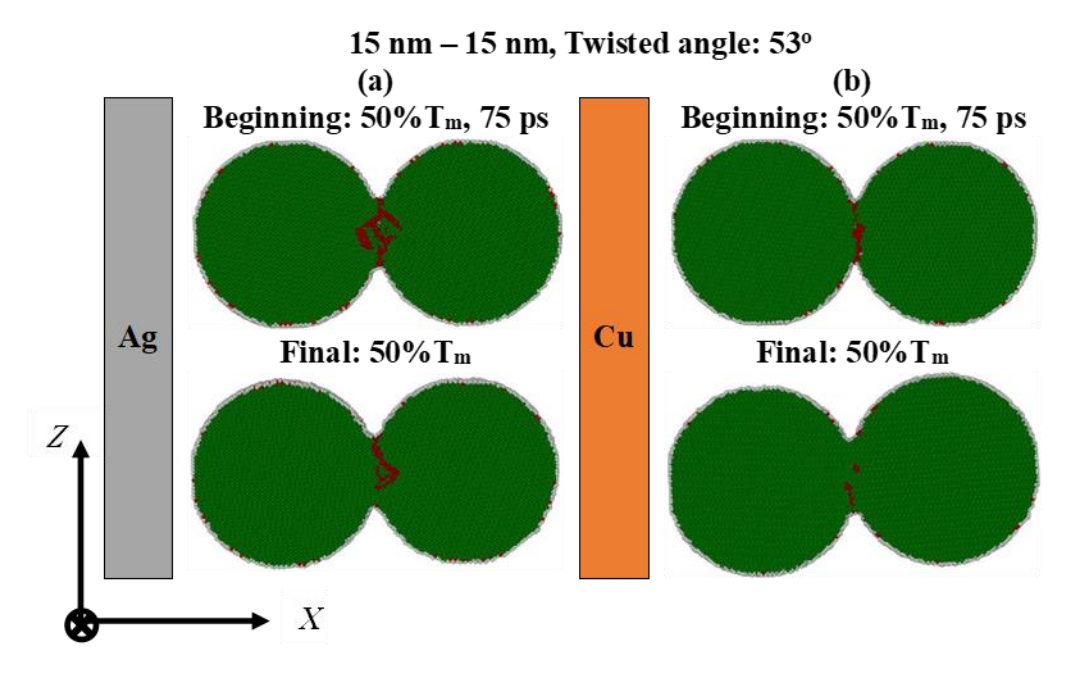


Figure 9 Examples of the resulting morphologies of equal-sized twisted NPs with a diameter of 15 nm at 50%T_m sintering temperatures: (a) Ag NPs with a twisted misorientation angle of 53.15° and (b) Cu NPs with a twisted misorientation angle of 53.15°.

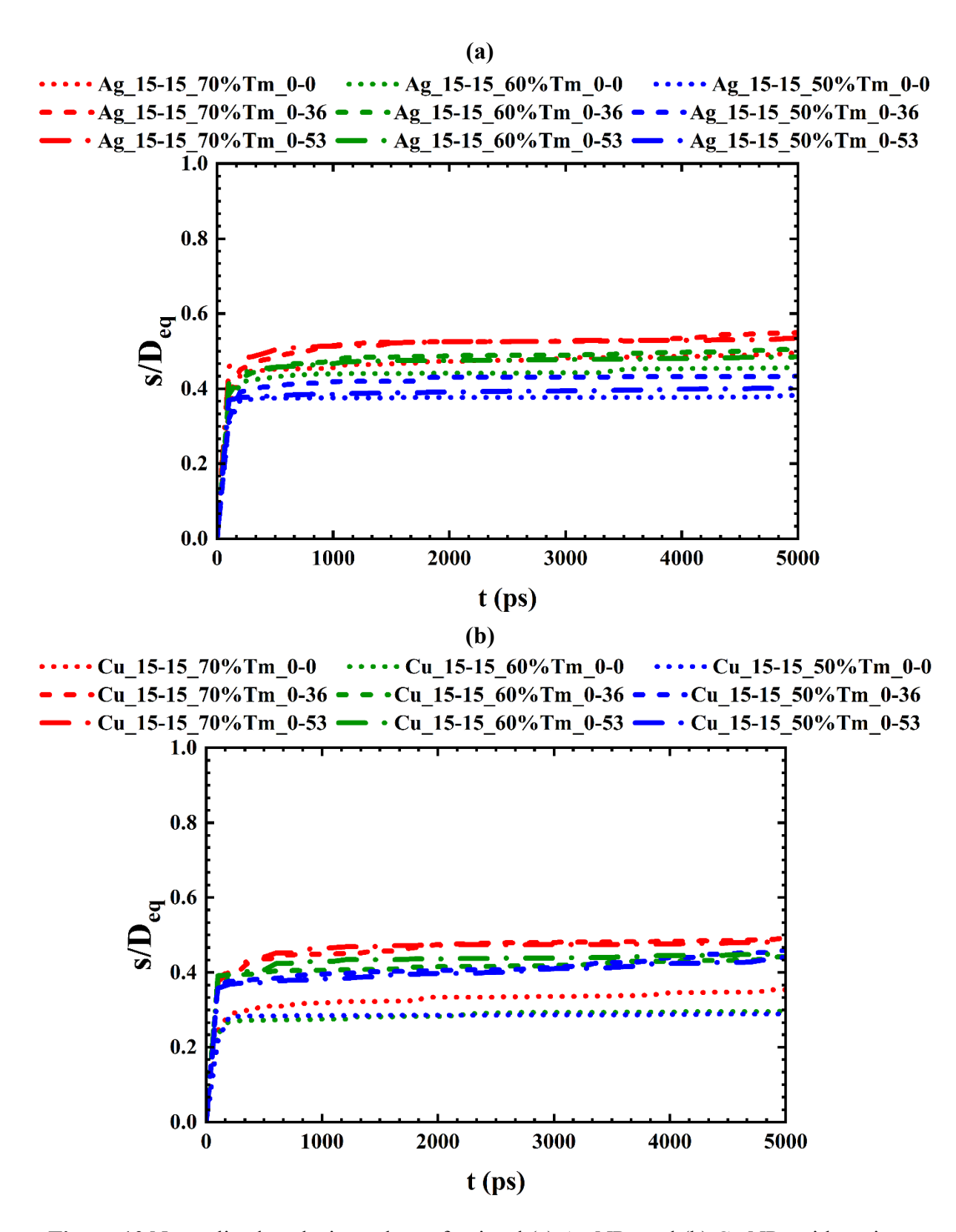


Figure 10 Normalized neck size values of twisted (a) Ag NPs and (b) Cu NPs with various misorientation angles at different temperatures as functions of time.

3.4 Predictive model of characteristic sintering time using MD simulations data

In this section, the sintering behavior of NPs presented in the previous sections (i.e., in **Figures** 4 and 6) was cast into a mathematical framework that could be used to predict the sintering effectiveness, quantified by characteristic sintering times. The characteristic sintering time (t_{ch}) was defined as the time required for the neck size between NPs to reach a significant fraction of particle diameter [62], i.e., a critical normalized neck size (s/D_{eq}). Essentially, the smaller the t_{ch} , the more effective the sintering. In this work, this critical value was selected based on sintering case that was the most effective among all the conditions considered, i.e., $s/D_{eq} = 0.93$ for the Ag_5-5_70%T_m_0-0 case, as it is shown in **Figure 4(a)**. For all other cases, it was assumed that the sintering was all able to reach the neck size of $s/D_{eq} = 0.93$ between NPs [62], should the simulation time be sufficient. In addition, it was assumed that all sintering relations of s/D_{eq} -t followed a generalized nonlinear relationship [63–65]; therefore, a nonlinear relationship between the squared normalized neck size and the duration of sintering was introduced:

$$\left(\frac{s}{D_{eq}}\right)^2 = \frac{a^2 b(\frac{t}{t_{ch}})}{1 + a b(\frac{t}{t_{ch}})} \tag{3}$$

where t and t_{ch} are sintering time and characteristic sintering time, respectively, and a and b are constants. When **Eq. 3** was fitted for the case of Ag_5-5_70%T_m_0-0, the fitted values of a and b were 0.84 and 109.15, respectively.

With the so-obtained constants a and b, the t_{ch} of all simulated cases could be estimated by substituting the s/D_{eq} by the end of simulations and the length of simulation (t = 5000 ps). For example, to obtain the characteristic sintering time for the case of Ag_5-5_60%Tm_0-0, its slp $s/D_{eq} = 0.81$ was mapped to the fitted **Eq. 3** (see the graphical illustration in **Figure 11**), and $t_{ch} = 4,9400,000$ ps was obtained when t = 5000 ps was substituted.

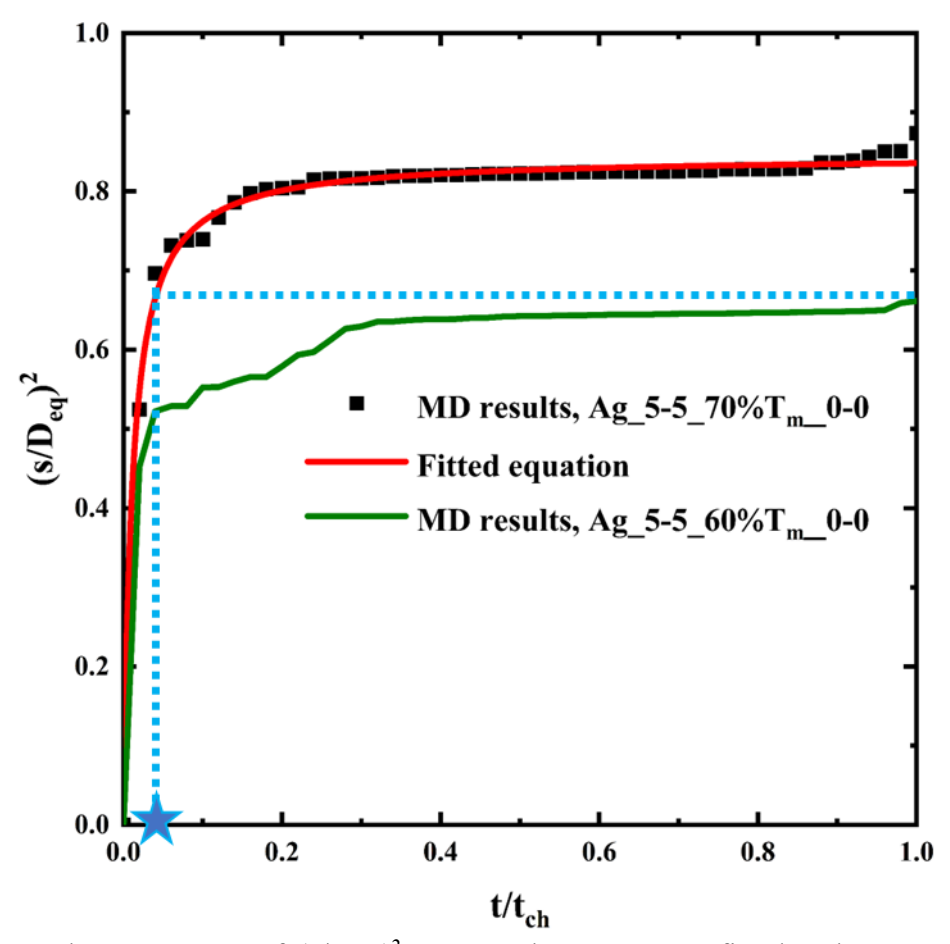


Figure 11 The appearance of $(x/Deq)^2$ -t curve when Eq. 3 was fitted to the case of Ag_5-5_70%Tm_0-0's and the schematic illustration of the procedure to obtain t_{ch} for other simulation cases.

Next, the characteristic sintering time (t_{ch}) was correlated with the NPs size (D_{eq}) and temperature (T). To this end, the general form of an explicit expression as a predictive model was adopted [63,66], requiring calibration of parameters to suit the unique sintering conditions, materials, and NP sizes, enabling a more accurate prediction of the sintering time. This explicit expression related the characteristic sintering time to a power function of NP diameter, indicating that smaller diameters generally resulted in more effective sintering, and to an exponential function of temperature, reflecting the strong influence of temperature on sintering:

$$t_{\rm ch} = A_1 D_{\rm eq}^{A_2} \exp\left(\frac{A_3}{kT}\right) \tag{4}$$

where A_1 is a pre-exponential diffusion coefficient and depends on sintering mechanisms and A_3 is proportional to the diffusion activation energy. **Table 3** lists the parametric values for **Eq. 4**, obtained by fitting the equation to the t_{ch} - D_{eq} - T data generated from the MD simulations and the analysis outlined in **Figure 11**. The higher values of A_3 for Cu NPs appeared to agree well with the higher values of diffusion activation energy for Cu NPs. Cu NPs and Ag NPs had A_2 values close to one and were of the same order of magnitude. The slightly higher values of A_2 for Ag NPs, compared to Cu NPs, indicated that Ag NPs' sintering effectiveness was more susceptible to particle size than Cu NPs.

Table 3 Parameter values in Eq. 4 obtained from the fitting procedure.

	$\mathbf{A_1}$	\mathbf{A}_{2}	A 3
Ag	12199.72 ps/nm ^{1.21}	1.21	0.0957 eV
Cu	38003.00 ps/nm ^{0.99}	0.99	0.1138 eV

In **Figure 2**, the characteristic sintering times from MD simulations of equal-sized NPs and unequal-sized NPs at different equivalent diameters and sintering temperatures are compared to the characteristic sintering times predicted by the model formulated in **Eq. 4** and **Table 3**. The results showed that cases with higher temperatures generally required significantly shorter characteristic sintering times at a certain equivalent diameter, indicating a strong temperature-dependence of the sintering process. Moreover, at a specific temperature, cases with a smaller equivalent diameter required a shorter sintering time. Comparing the sintering behavior of Cu NPs and Ag NPs, it was found that Cu NPs required longer sintering times compared to Ag NPs, consistent with the arguments provided in *Section 3.1* regarding the higher diffusion activation energy and cohesive energy of Cu. The formation of GBs, as demonstrated in *Section 3.3*, fascilitated sintering in the presence of misorientation angles. Even with GBs, the effects of temperature and size remained consistent, i.e., sintering was more effective for smaller size NPs

and at higher temperatures, resulting in identical mathematical treatment as outlined above, to obtain sintering effciency, although fitting parameters could differ.

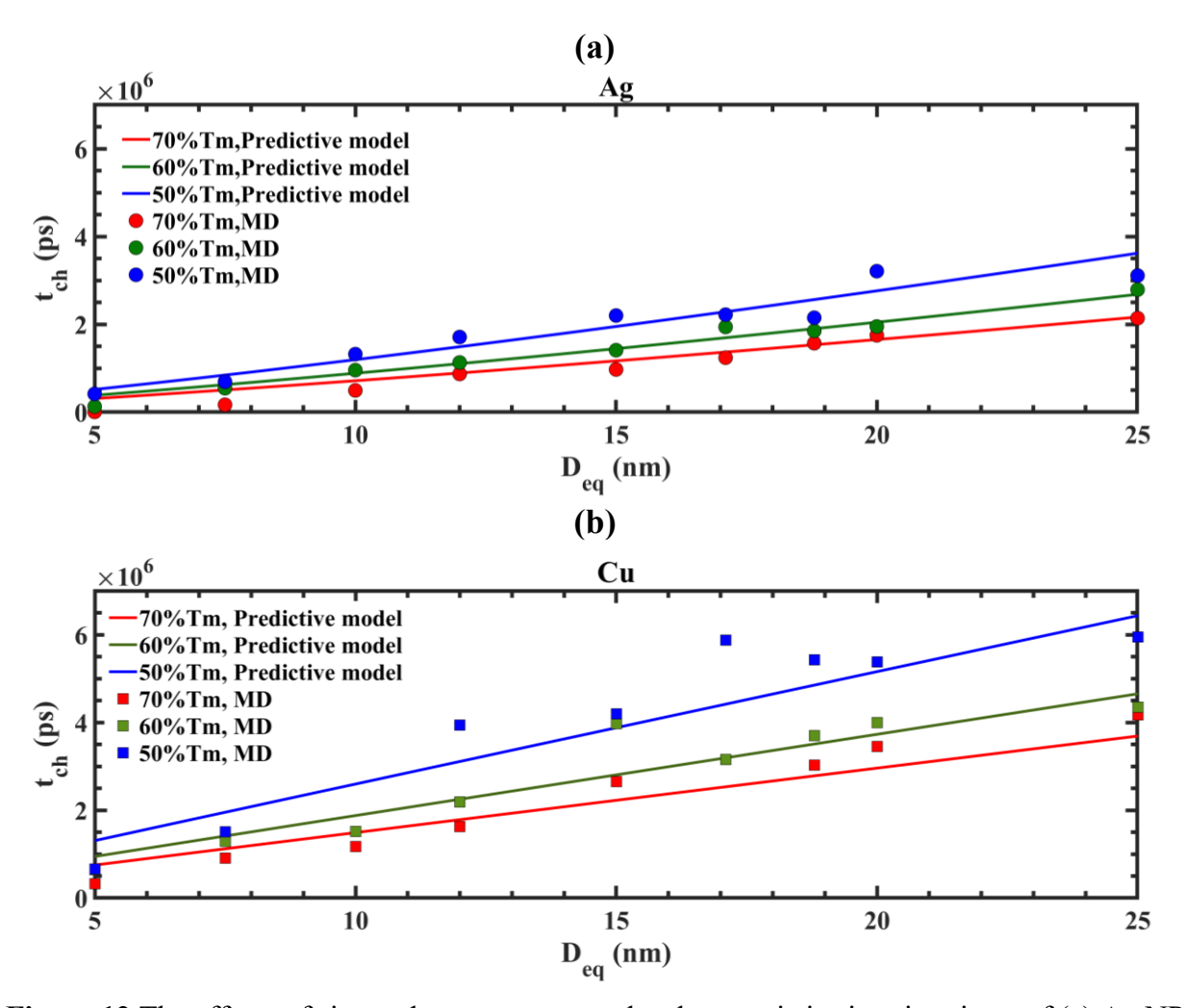


Figure 12 The effects of size and temperature on the characteristic sintering times of (a) Ag NPs and (b) Cu NPs are compared between MD data (markers) and predictive model (solid lines).

4. Conclusion

This work investigated the sintering behavior of a doublet of Ag NPs and Cu NPs with various sizes, particle size ratios, and misorientation angles under various sintering temperatures using molecular dynamics simulations. MD simulations provided valuable insights into the detailed spatiotemporal information through atomistic snapshots of the morphologies of the NPs during the sintering process that was difficult to obtain directly from experimental measurements due to the small length scale and short time scale tied to NP sintering. The sintering effectiveness was quantified by the normalized doublet neck size at the end of simulations, which in turn determined the characteristic sintering time. The following conclusions were drawn:

- 1. In general, smaller NPs sintered more effective due to their higher fractions of surface atoms, providing more effectiveness diffusion pathways and shorter diffusion paths from each NP to the neck region. In a pair of unequal-sized NPs, increasing particle size ratios expedited sintering due to differences in the pressure induced by surface tension.
- 2. NPs containing tilted and twisted misorientation angles sintered more effective than NPs without such misorientation angles forming GBs between the two adjacent NPs. This was due to GBs having lower diffusion activation energy. Sintering effectiveness was the highest in NPs with tilted misorientation angles, since GBs formed in NPs with the tilted misorientation angles were stable, whereas GBs formed in NPs with twisted misorientation angles destabilized and disappeared. Moreover, since Ag has a lower diffusion activation energy than Cu, Ag NPs sintered more effective than Cu NPs.
- 3. Overall, a higher sintering temperature positively affected sintering due to more mobile atoms. However, for the same amount of a rise in temperature, different sintering conditions showed different levels of increase in sintering effectiveness.

4. A predictive model to determine characteristic sintering time as a function of temperature and particle size was introduced for each material. The predictive model fitted the MD simulation data well and highlighted the interplay among different factors that influence sintering characteristics.

Acknowledgments

This work was supported by the U.S. National Science Foundation (NSF) under grant No. 2134024.

References

- [1] Z. Ahmadi, S. Lee, A. Patel, R.R. Unocic, N. Shamsaei, M. Mahjouri-Samani, Dry Printing and Additive Nanomanufacturing of Flexible Hybrid Electronics and Sensors, Adv. Mater. Interfaces. 9 (2022) 1–10. https://doi.org/10.1002/admi.202102569.
- [2] Z. Ahmadi, S. Lee, R.R. Unocic, N. Shamsaei, M. Mahjouri-Samani, Additive Nanomanufacturing of Multifunctional Materials and Patterned Structures: A Novel Laser-Based Dry Printing Process, Adv. Mater. Technol. 6 (2021). https://doi.org/10.1002/admt.202001260.
- [3] T. Liang, R.K. Pal, X. Zou, A. Root, A.D. Mazzeo, M.M. Hussain, N. El-Atab, Flexible and Stretchable Paper-based Structures for Electronic Applications, in: Handb. Flex. Stretchable Electron., CRC Press Boca Raton, FL, USA, 2019: pp. 337–375.
- [4] R. Martins, D. Gaspar, M.J. Mendes, L. Pereira, J. Martins, P. Bahubalindruni, P. Barquinha, E. Fortunato, Papertronics: Multigate paper transistor for multifunction applications, Appl. Mater. Today. 12 (2018) 402–414. https://doi.org/10.1016/J.APMT.2018.07.002.
- [5] L. Zhang, P. Feng, S. Xie, Y. Wang, Z. Ye, Z. Fu, Q. Wang, X. Ma, J. Zhang, P. He, K. Li, W. Zhao, Low-temperature sintering of silver nanoparticles on paper by surface modification, Nanotechnology. 30 (2019) 505303. https://doi.org/10.1088/1361-6528/ab437a.
- [6] R.M. German, Chapter One Introduction, in: R.M.B.T.-S. from E.O. to S.P. German (Ed.), Butterworth-Heinemann, Boston, 2014: pp. 1–12. https://doi.org/https://doi.org/10.1016/B978-0-12-401682-8.00001-X.
- [7] Y. Yang, Z. Li, S. Yang, Y. Li, J. Huang, Multiscale simulation study of laser sintering of inkjet-printed silver nanoparticle inks, Int. J. Heat Mass Transf. 159 (2020). https://doi.org/10.1016/j.ijheatmasstransfer.2020.120110.
- [8] C. Qian, K. Hu, H. Wang, L. Nie, Q. Feng, Z. Lu, P. Li, K. Lu, The effect of particle size distribution on the microstructure and properties of Al2O3 ceramics formed by stereolithography, Ceram. Int. 48 (2022) 21641–21650. https://doi.org/10.1016/J.CERAMINT.2022.04.133.
- [9] A. Molinari, Fundamentals of Sintering: Solid State Sintering, Encycl. Mater. Met. Alloy. (2021) 471–480. https://doi.org/10.1016/B978-0-12-819726-4.00096-X.
- [10] J. Pan, H. Le, S. Kucherenko, J.A. Yeomans, A model for the sintering of spherical particles of different sizes by solid state diffusion, Acta Mater. 46 (1998) 4671–4690. https://doi.org/10.1016/S1359-6454(98)00144-X.
- [11] F. Parhami, R.M. McMeeking, A.C.F. Cocks, Z. Suo, A model for the sintering and coarsening of rows of spherical particles, Mech. Mater. 31 (1999) 43–61. https://doi.org/10.1016/S0167-6636(98)00049-0.
- [12] B.P. Uberuaga, L.J. Vernon, E. Martinez, A.F. Voter, The relationship between grain boundary structure, defect mobility and grain boundary sink efficiency, Sci. Reports 2015

- 51. 5 (2015) 1–9. https://doi.org/10.1038/srep09095.
- [13] H. Ichinose, G.G. Kuczynski, Role of grain boundaries in sintering, Acta Metall. 10 (1962) 209–213. https://doi.org/10.1016/0001-6160(62)90118-9.
- [14] J.E. BURKE, Role of Grain Boundaries in Sintering., J. Am. Ceram. Soc. 40 (1957) 80–85. https://doi.org/10.1111/J.1151-2916.1957.TB12580.X.
- [15] R.M. German, Sintering: from empirical observations to scientific principles, n.d.
- [16] S.-J.L. Kang, 4 INITIAL STAGE SINTERING, in: S.-J.L.B.T.-S. Kang (Ed.), Butterworth-Heinemann, Oxford, 2005: pp. 39–55. https://doi.org/https://doi.org/10.1016/B978-075066385-4/50004-2.
- [17] D.L. JOHNSON, I.B. CUTLER, Diffusion Sintering: I, Initial Stage Sintering Models and Their Application to Shrinkage of Powder Compacts, J. Am. Ceram. Soc. 46 (1963) 541–545. https://doi.org/10.1111/J.1151-2916.1963.TB14606.X.
- [18] H. Pan, S.H. Ko, C.P. Grigoropoulos, The solid-state neck growth mechanisms in low energy laser sintering of gold nanoparticles: A Molecular dynamics simulation study, J. Heat Transfer. 130 (2008). https://doi.org/10.1115/1.2943303.
- [19] A. Kobata, K. Kusakabe, S. Morooka, Growth and transformation of TiO2 crystallites in aerosol reactor, AIChE J. 37 (1991) 347–359.
- [20] T. Seto, M. Shimada, K. Okuyama, Evaluation of Sintering of Nanometer-Sized Titania Using Aerosol Method, Aerosol Sci. Technol. 23 (1995) 183–200. https://doi.org/10.1080/02786829508965303.
- [21] B. Buesser, A.J. Gr€ Ohn, S.E. Pratsinis, Sintering Rate and Mechanism of TiO 2 Nanoparticles by Molecular Dynamics, J. Phys. Chem. C. 115 (2011) 11030–11035. https://doi.org/10.1021/jp2032302.
- [22] G. Yang, H. Lai, W. Lin, J. Tong, J. Cao, J. Luo, Y. Zhang, C. Cui, A quantitative model to understand the microflow-controlled sintering mechanism of metal particles at nanometer to micron scale, (2021). https://doi.org/10.1088/1361-6528/ac232d.
- [23] X. Long, B. Hu, Y. Feng, C. Chang, M. Li, Correlation of microstructure and constitutive behaviour of sintered silver particles via nanoindentation, Int. J. Mech. Sci. 161–162 (2019). https://doi.org/10.1016/J.IJMECSCI.2019.105020.
- [24] M. Gu, T. Liu, X. Xiao, G. Li, W. Liao, Simulation and Experimental Study of the Multisized Silver Nanoparticles Sintering Process Based on Molecular Dynamics, (2022). https://doi.org/10.3390/nano12061030.
- [25] S. Zhang, Q. Wang, T. Lin, P. Zhang, P. He, K.W. Paik, Cu-Cu joining using citrate coated ultra-small nano-silver pastes, J. Manuf. Process. 62 (2021) 546–554. https://doi.org/10.1016/J.JMAPRO.2020.11.043.
- [26] R. Theissmann, M. Fendrich, R. Zinetullin, G. Guenther, G. Schierning, D.E. Wolf, Crystallographic reorientation and nanoparticle coalescence, (n.d.). https://doi.org/10.1103/PhysRevB.78.205413.

- [27] M.A. Asoro, P.J. Ferreira, D. Kovar, In situ transmission electron microscopy and scanning transmission electron microscopy studies of sintering of Ag and Pt nanoparticles, Acta Mater. 81 (2014) 173–183. https://doi.org/10.1016/J.ACTAMAT.2014.08.028.
- [28] M. Song, G. Zhou, N. Lu, J. Lee, E. Nakouzi, H. Wang, D. Li, Oriented attachment induces fivefold twins by forming and decomposing high-energy grain boundaries, (n.d.).
- [29] T. Matsuda, Development of a DEM taking account of neck increments caused by surface diffusion for sintering and application to analysis of the initial stage of sintering, Comput. Mater. Sci. 196 (2021). https://doi.org/10.1016/J.COMMATSCI.2021.110525.
- [30] R.K. Bordia, S.J.L. Kang, E.A. Olevsky, Current understanding and future research directions at the onset of the next century of sintering science and technology, J. Am. Ceram. Soc. 100 (2017) 2314–2352. https://doi.org/10.1111/JACE.14919.
- [31] A. Malti, A. Kardani, A. Montazeri, An insight into the temperature-dependent sintering mechanisms of metal nanoparticles through MD-based microstructural analysis, Powder Technol. 386 (2021) 30–39. https://doi.org/10.1016/J.POWTEC.2021.03.037.
- [32] J. Nandy, N. Yedla, P. Gupta, H. Sarangi, S. Sahoo, Sintering of AlSi10Mg particles in direct metal laser sintering process: A molecular dynamics simulation study, Mater. Chem. Phys. 236 (2019) 121803. https://doi.org/10.1016/J.MATCHEMPHYS.2019.121803.
- [33] J. Nandy, S. Sahoo, H. Sarangi, Study on shape dependency of Al-alloy nanoparticles during coalescence in direct metal laser sintering: A molecular dynamics approach, Mater. Today Proc. 41 (2021) 347–351. https://doi.org/10.1016/J.MATPR.2020.09.557.
- [34] J.M. Sestito, F. Abdeljawad, T.A.L. Harris, Y. Wang, A. Roach, An atomistic simulation study of nanoscale sintering: The role of grain boundary misorientation, Comput. Mater. Sci. 165 (2019) 180–189. https://doi.org/10.1016/j.commatsci.2019.04.015.
- [35] Modelling sintering at particle scale using variational and molecular dynamic methods ANAS OBEED ALSHAMMERY, 2018.
- [36] P. Zeng, S. Zajac, P.C. Clapp, J.A. Rifkin, Nanoparticle sintering simulations, Mater. Sci. Eng. A. 252 (1998) 301–306. https://doi.org/10.1016/S0921-5093(98)00665-0.
- [37] M. Gu, T. Liu, X. Xiao, G. Li, W. Liao, Simulation and Experimental Study of the Multisized Silver Nanoparticles Sintering Process Based on Molecular Dynamics, Nanomaterials. 12 (2022). https://doi.org/10.3390/NANO12061030/S1.
- [38] S.H. Ko, C.P. Grigoropoulos, S.H. Ko Costas, P. Grigoropoulos, The Solid-State Neck Growth Mechanisms in Low Energy Laser Sintering of Gold Nanoparticles: A Molecular Dynamics Simulation Study Mechanical Metamaterials Design View project Direct Laser Writing Process View project Heng Pan The Solid-State Neck Growth Mechanisms in Low Energy Laser Sintering of Gold Nanoparticles: A Molecular Dynamics Simulation Study, Artic. J. Heat Transf. (2008). https://doi.org/10.1115/1.2943303.
- [39] P. Ghosh, J. Lu, Z. Chen, H. Yang, M. Qiu, Q. Li, Photothermal-Induced Nanowelding of Metal—Semiconductor Heterojunction in Integrated Nanowire Units, Adv. Electron. Mater. 4 (2018). https://doi.org/10.1002/AELM.201700614.

- [40] K. Sisáková, · A Oriňak, · R Oriňaková, · M Strečková, · J Patera, · A Welle, · Z Kostecká, · V Girman, Methane Decomposition Over Modified Carbon Fibers as Effective Catalysts for Hydrogen Production, Catal. Letters. 150 (2020) 781–793. https://doi.org/10.1007/s10562-019-02962-w.
- [41] X.M. Wei, J.M. Zhang, K.W. Xu, The energy and structure of (0 0 1) twist grain boundary in noble metals, Appl. Surf. Sci. 253 (2006) 854–858. https://doi.org/10.1016/j.apsusc.2006.01.019.
- [42] A. Ayadi, H. Laib, O. Khalfallah, Relationship between structure and energy of symmetric tilt grain boundaries in Ag and Ni, Acta Phys. Pol. A. 138 (2020) 528–532. https://doi.org/10.12693/APhysPolA.138.528.
- [43] S. Shao, J. Wang, A. Misra, R.G. Hoagland, Spiral patterns of dislocations at nodes in (111) semi-coherent FCC interfaces, Sci. Rep. 3 (2013). https://doi.org/10.1038/SREP02448.
- [44] M.I. Mendelev, A.H. King, The interactions of self-interstitials with twin boundaries, Philos. Mag. 93 (2013) 1268–1278. https://doi.org/10.1080/14786435.2012.747012.
- [45] X.W. Zhou, R.A. Johnson, H.N.G. Wadley, Misfit-energy-increasing dislocations in vapor-deposited CoFe/NiFe multilayers, Phys. Rev. B. 69 (2004) 144113. https://doi.org/10.1103/PhysRevB.69.144113.
- [46] P.-H. Huang, P.-C. Hsu, T.-H. Huang, C.-S. Chou, Laser sintering of Cu nanoparticles: analysis based on modified continuum-atomistic model, Appl. Phys. A. 126 (2019) 31. https://doi.org/10.1007/s00339-019-3213-5.
- [47] A.J. Haslam, S.R. Phillpot, D. Wolf, D. Moldovan, H. Gleiter, Mechanisms of grain growth in nanocrystalline fcc metals by molecular-dynamics simulation, Mater. Sci. Eng. A. 318 (2001) 293–312. https://doi.org/10.1016/S0921-5093(01)01266-7.
- [48] D. Nelli, M. Cerbelaud, R. Ferrando, C.E. Minnai, Tuning the coalescence degree in the growth of Pt-Pd nanoalloys, (2021). https://doi.org/10.1039/d0na00891e.
- [49] A.P. Thompson, H.M. Aktulga, R. Berger, D.S. Bolintineanu, W.M. Brown, P.S. Crozier, P.J. in 't Veld, A. Kohlmeyer, S.G. Moore, T.D. Nguyen, R. Shan, M.J. Stevens, J. Tranchida, C. Trott, S.J. Plimpton, LAMMPS a flexible simulation tool for particle-based materials modeling at the atomic, meso, and continuum scales, Comput. Phys. Commun. 271 (2022). https://doi.org/10.1016/J.CPC.2021.108171.
- [50] L. Ding, R.L. Davidchack, J. Pan, A molecular dynamics study of sintering between nanoparticles, Comput. Mater. Sci. 45 (2009) 247–256. https://doi.org/10.1016/j.commatsci.2008.09.021.
- [51] W. Humphrey, A. Dalke, K. Schulten, VMD: Visual molecular dynamics, J. Mol. Graph. 14 (1996) 33–38. https://doi.org/10.1016/0263-7855(96)00018-5.
- [52] A. Stukowski, Visualization and analysis of atomistic simulation data with OVITO-the Open Visualization Tool, Model. Simul. Mater. Sci. Eng. 18 (2010). https://doi.org/10.1088/0965-0393/18/1/015012.

- [53] A.S. Malek, A. Elnahrawy, H. Anwar, You may also like Automated detection of premature ventricular contraction in ECG signals using enhanced template matching algorithm, (2016). https://doi.org/10.1088/0965-0393/24/5/055007.
- [54] Z. Li, S. Shao, N. Li, K. Mccall, J. Wang, S.X. Zhang, Single Crystalline Nanostructures of Topological Crystalline Insulator SnTe with Distinct Facets and Morphologies, (2023). https://doi.org/10.1021/nl4030193.
- [55] M. Chandross, Energetics of the formation of Cu-Ag core—shell nanoparticles, Model. Simul. Mater. Sci. Eng. 22 (2014). https://doi.org/10.1088/0965-0393/22/7/075012.
- [56] Y. Mishin, M.J. Mehl, D.A. Papaconstantopoulos, A.F. Voter, J.D. Kress, Structural stability and lattice defects in copper: Ab initio, tight-binding, and embedded-atom calculations, (n.d.). https://doi.org/10.1103/PhysRevB.63.224106.
- [57] K. Kambe, Cohesive energy of noble metals, Phys. Rev. 99 (1955) 419–422. https://doi.org/10.1103/PhysRev.99.419.
- [58] H. Zhu, R.S. Averback, Sintering processes of two nanoparticles: A study by molecular dynamics simulations, Philos. Mag. Lett. 73 (1996) 27–33. https://doi.org/10.1080/095008396181073.
- [59] P. Zeng, S. Zajac, P.C. Clapp, J.A. Rifkin, Nanoparticle sintering simulations 1, Mater. Sci. Eng. 252 (1998) 301–306.
- [60] H.A. Alarifi, M. Atis, C. Özdoğan, A. Hu, M. Yavuz, Y. Zhou, Molecular Dynamics Simulation of Sintering and Surface Premelting of Silver Nanoparticles, (2013). https://doi.org/10.2320/matertrans.MD201225.
- [61] SYNTHESIS AND CHARACTERIZATION OF BIMETALLIC GOLD-SILVER (AuAg) NANOCATALYST VIA SEED COLLOID TECHNIQUE NURAFALIANA BINTI
 BERAHIM DISSERTATION SUBMITTED IN FULFILMENT OF THE
 REQUIREMENTS FOR THE DEGREE OF MASTER OF ENGINEERING SCIENCE,
 (n.d.).
- [62] B. Buesser, A.J. Gröhn, S.E. Pratsinis, Sintering rate and mechanism of TiO2 nanoparticles by molecular dynamics, J. Phys. Chem. C. 115 (2011) 11030–11035. https://doi.org/10.1021/JP2032302.
- [63] T. Seto, M. Shimada, K. Okuyama, Evaluation of sintering of nanometer-sized titania using aerosol method, Aerosol Sci. Technol. 23 (1995) 183–200. https://doi.org/10.1080/02786829508965303.
- [64] W. Koch, S.K. Friedlander, The effect of particle coalescence on the surface area of a coagulating aerosol, J. Colloid Interface Sci. 140 (1990) 419–427. https://doi.org/10.1016/0021-9797(90)90362-R.
- [65] J. Wang, X. Guo, Adsorption kinetic models: Physical meanings, applications, and solving methods, J. Hazard. Mater. 390 (2020) 122156. https://doi.org/10.1016/J.JHAZMAT.2020.122156.
- [66] A. Kobata, K. Kusakabe, S. Morooka, Growth and Transformation of Ti02 Crystallites in

Aerosol Reactor, (n.d.). https://doi.org/10.1002/aic.690370305.